



## ORIGINAL ARTICLE

# Silver-platinum bimetallic nanoparticles as heterogeneous persulfate activator for the oxidation of malachite green



Abeer Mohammed Al-Balawi, Zoya Zaheer\*, Samia A. Kosa

Department of Chemistry, Faculty of Science, King Abdulaziz University, P. O. Box 80203, Jeddah 21589, Saudi Arabia

Received 31 January 2023; accepted 23 March 2023

Available online 30 March 2023

## KEYWORDS

Ag-Pt;  
Bimetallic;  
K<sub>2</sub>S<sub>2</sub>O<sub>8</sub>;  
Malachite green;  
Chemical oxidation

**Abstract** Fabrication of noble metal nanoparticles by using green chemical method with plant extract as reducing agent to the in situ oxidation toxic water contaminants have been the subject of various investigators due to their enhanced catalytic efficiencies. This paper describes the extraction of caffeic acid from *Artemisia herba-alba* aqueous extract, and preparation of silver (Ag), platinum (Pt), and silver-platinum (Ag-Pt) nanoparticles with caffeic acid as a reducing and capping agent. The as-prepared Ag-Pt NPs was used as a heterogeneous activator of persulphate (K<sub>2</sub>S<sub>2</sub>O<sub>8</sub>) for the in situ chemical oxidation of malachite green (MG). The Ag-Pt NPs shows no surface Plasmon resonance absorption band. The malachite green dye was completely decolorized in presence of Ag-Pt/K<sub>2</sub>S<sub>2</sub>O<sub>8</sub> system. SO<sub>4</sub><sup>•-</sup> and HO<sup>•</sup> radicals generated by the cleavage of S<sub>2</sub>O<sub>8</sub><sup>2-</sup> peroxide activation with Ag-Pt were responsible for the MG decolorization as well as mineralization. The Ag-Pt NPs acted as a sacrificial electron donor. The Ag-Pt NPs were characterized by using conventional techniques such as, UV-visible, FTIR, SEM, TEM, EDX, XPS, and XRD spectroscopic methods.

© 2023 The Author(s). Published by Elsevier B.V. on behalf of King Saud University. This is an open access article under the CC BY-NC-ND license (<http://creativecommons.org/licenses/by-nc-nd/4.0/>).

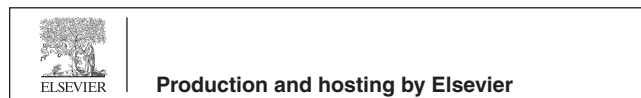
## 1. Introduction

*Artemisia herba-alba* was known for medicinal and therapeutic properties due to the presence of many bioactive compounds such as

\* Corresponding author.

E-mail addresses: [zoya.zaheer@gmail.com](mailto:zoya.zaheer@gmail.com), [zzkhan@kau.edu.sa](mailto:zzkhan@kau.edu.sa) (Z. Zaheer).

Peer review under responsibility of King Saud University.



flavonoids, sesquiterpenes, and polyphenolic acids. Herbal tea from *artemisia herba-alba* has been used as analgesic, antibacterial, antispasmodic, antioxidant, hemostatic, and nematocidal agents (Al-Shamaony et al., 1994; Boriky et al., 1996; Laid et al., 2008). Caffeic acid is one of the most water soluble common phenolic acid of *Artemisia herba-alba*, and used in coffee, tea, olive oil and wine (Iglesias et al., 2009; Gulcin, 2006). The aqueous extract of *Artemisia herba-alba* increased gastro-intestinal transit time. Generally, the aqueous extract of various parts of natural plants (Irvani, 2011), fruits (Ghodake et al., 2010), green tea (Zaheer et al., 2019), betanin (Kosa and Zaheer, 2019), flowers (Shankar et al., 2003), and biomass (Gardea-Torresdy et al., 2003) were used to the fabrication of nanomaterials. Bakshi and his coworkers reported the synthesis of nanomaterials by using different natural and synthetic stabilizers for different

applications (Bakshi, 2014; Bakshi, 2018; Gurtu et al., 2020). The natural biomolecules present in an aqueous extract acted as a capping agents and avoid the necessity of externally added stabilizer for the protection the nanoparticles aggregation (Riedesel et al., 2021).

Advanced oxidation technologies (hydroxyl and sulfate free radical based) are ecofriendly and based on the generation of reactive radical species ( $\text{HO}^\bullet$  and  $\text{SO}_4^{\bullet-}$ ). Persulfate is a solid strong oxidant ( $E^0 = 2.01 \text{ V}$ ) than hydrogen peroxide ( $E^0 = 1.76 \text{ V}$ ). It is highly stable at ambient temperature, easy to transport and relatively low cost. Generally, transition metals and metal nanoparticles were used as peroxide bond activator to the generation of radical species for the wastewater treatment (Anipsitakis and Dionysiou, 2004; Xu and Li, 2010; Deng et al., 2008; Oh et al., 2009; Al-Shehri et al., 2021; Park et al., 2018). For example, Anipsitakis and Dionysiou were used different metal ions such as  $\text{Ag}^+$ ,  $\text{Co}^{2+}$ ,  $\text{Cu}^{2+}$ ,  $\text{Fe}^{2+}$ ,  $\text{Mn}^{2+}$ ,  $\text{Ni}^{2+}$ ,  $\text{Ce}^{3+}$ ,  $\text{Fe}^{3+}$ ,  $\text{V}^{3+}$ , and  $\text{Ru}^{3+}$  to the generation of reactive inorganic radicals by the activation of three oxidants, namely, hydrogen peroxide, potassium peroxymonosulfate, and persulfate (Anipsitakis and Dionysiou, 2004).

Literature contained abundant reports and reviews regarding the applications and importance of using biorenewable resources in bio-fuels from natural biomass (Singh et al., 2022), organic waste reagents in synthetic chemistry (Venkateswarlu et al., 2021), greenhouse gas emissions in BIMSTEC region (Sharma et al., 2021), magnetic nanoparticles for wastewater treatment (Vallinayagam et al., 2021), and biomass derived catalyst for the oxidation of  $\alpha$ -hydroxy ketones (Naidu et al., 2022). The reduced graphene oxide/ $\text{ZnFe}_2\text{O}_3$  (Rani et al., 2017), graphene oxide(RGO)/ $\text{Fe}_3\text{O}_4$  (Vinothkannan et al., 2015) nanocomposites were prepared and used as an efficient catalyst for the degradation of methylene blue under different experimental conditions. The bio-assisted,  $\beta$ -cyclodextrin-functionalized, and piper betle biomass capped silver NPs were prepared and used as sensor for the colorimetric and selective detection of copper(II), melamine, and nitrite, respectively (Kirubaharan et al., 2012; Xavier et al., 2014; Ramachandaran et al. 2016). The carbon nanodots were prepared using lemon and utilized for the selective and sensitive detection of Fe(III) ions (Xavier et al., 2019). Bio-assisted synthesis of platinum (Mohamadi et al., 2020), silver (Asadi et al., 2018), and CdO NPs (Kaveh et al., 2021) were reported by using the natural plant extract. The platinum and CdO NPs were used as sensor for the detection of hydrogen peroxide and quantification of cefixime, respectively.

Xu and Li reported the degradation of orange G azo dye using  $\text{HO}^\bullet$  reactive oxygen species generated by  $\text{K}_2\text{S}_2\text{O}_8$ /ferrous ions (Xu and Li, 2010). These investigators also discussed the role of inorganic salts ( $\text{Cl}^-$ ,  $\text{NO}_3^-$ ,  $\text{HCO}_3^-$ , and  $\text{H}_2\text{PO}_4^-$ ) on the rates of dye degradation.  $\text{Co}_3\text{O}_4$ -N doped carbon nanotubes were used as persulfate activation catalyst to the in situ chemical decomposition of azo dyes (Jiang et al., 2020). Various mono-, and bimetallic nanomaterials such as  $\text{Co}_3\text{O}_4$ ,  $\text{Co}(\text{OH})_2$ ,  $\text{CuO}$ ,  $\text{Fe}_3\text{O}_4$ ,  $\text{ZnO}$ ,  $\text{CuFe}_2\text{O}_4$ ,  $\text{Mn}_3\text{O}_4$ ,  $\text{CoFe}_2\text{O}_4$ ,  $\text{MnFe}_2\text{O}_4$ , and carbon nanotubes have been used to the generation of  $\text{SO}_4^{\bullet-}$ , and  $\text{HO}^\bullet$  radicals for the removal of wastewater contaminants (Yao et al., 2013; Al-Anazi et al., 2018; Lee et al., 2015; Zhu et al., 2013; Zhu et al., 2011). Ultrasound radiations combined with heterogeneous titanium oxide and homogenous photocatalysis method was used for the oxidation of MG in water (Berberidou et al., 2007). Hameed and Lee reported the degradation of malachite green by using Fenton's reagent ( $\text{Fe}^{2+} + \text{H}_2\text{O}_2$ ) for the generation of  $\text{HO}^\bullet$  reactive species (Hameed and Lee, 2009). Wu et al. utilized the iron NPs as a catalyst for the heterogeneous oxidation of MG with  $\text{H}_2\text{O}_2$  (Wu et al., 2015). The  $\text{Fe}_3\text{O}_4$ /graphene aerogels and  $\text{CuFe}_2\text{O}_4$ @biochar composite were used as  $\text{S}_2\text{O}_8^{2-}$  activators for the degradation of MG (Lu et al., 2020; Huang et al., 2021). The use of Ag-Pt bimetallic as a heterogeneous  $\text{S}_2\text{O}_8^{2-}$  activator has not been reported in the literature for the in situ chemical oxidation of toxic MG at room temperature.

Caffeic acid (3,4-dihydroxycinnamic acid) isolated from the aqueous extract of *Artemisia herba-alba* at room temperature, and used for the fabrication of Ag, Pt, and Ag-Pt NPs for the first time. We determined the catalytic efficiency of Ag-Pt in the heterogeneous activation

of  $\text{K}_2\text{S}_2\text{O}_8$  for the degradation of MG (triphenyl methane basic dye, widely used in food and dyeing industries as coloring agent, and difficult to remove from wastewater). The main objectives of this study were to provide (i) simple cost effective green method for the synthesis of Ag-Pt NPs using natural medicinal plant and (ii) insights into the kinetics of dye degradation by  $\text{SO}_4^{\bullet-}$  based advanced oxidation processes under environmentally relevant conditions. Bimetallic Ag-Pt acted as an excellent heterogeneous  $\text{S}_2\text{O}_8^{2-}$  activator for the in situ chemical oxidation of MG at 25 °C within 50 min of reaction time.

## 2. Experimental section

### 2.1. Materials

The aerial parts of *Artemisia herba-alba* were collected from plants growing wild in Yanbo region of Saudi Arabia, dried in dark at room temperature, ground to fine powder by using an electric mill, and conversed in a desiccator. Metal salt precursor (silver nitrate and potassium tetrachloroplatinate ( $\text{K}_2\text{-PtCl}_4$ , molar mass = 415.09 g/mol  $\geq 99.9\%$ )), potassium persulfate, malachite green, sodium hydroxide, and other chemicals were used as received. Deionized water was used as solvent to the preparation of all reagents solution. Silver nitrate solution was stored in a brown glass container to prevent the photochemical reactions. Methanol, tertiary butyl alcohol, and potassium iodide were employed to scavenge the formation of reactive radical species.

### 2.2. Extraction of caffeic acid

For the extraction of caffeic acid, the 10.0 g of dry powder of *Artemisia herba-alba* plant was taken in a stoppered round bottom reaction vessel flask. The 250 mL of deionized water into the vessel, and the solution was heated for 60 min at 70 °C with constant stirring. The resulting reaction mixture was kept for 24 h at 25 °C for complete extraction of caffeic acid, filtered through a Whatmam filter paper, and pale yellow color solution stored in an amber glass container until analyzed. The photo images of *Artemisia herba-alba*, dry plant, and resulting pale yellow extract are given in Scheme 1. UV-visible spectra of pale yellow color was measured in the range of 200 to 800 nm on the UV-visible spectrophotometer, and compared with an authentic sample of caffeic acid purchased from the Sigma-Aldrich.

### 2.3. Synthesis of Ag, Pt, and Ag-Pt NPs

Green chemical reduction method was utilized for the synthesis of water soluble silver and platinum sols at room temperature. *Artemisia herba-alba* plant water extract was employed as reducing and capping agent (Zaheer et al., 2019). In order to prepare water soluble silver sols (Ag NPs), the required amount of silver nitrate and an aqueous extract of plant were placed into the vial, and required volume of deionized water was added for dilution. The pale yellow to dark brown color appeared as the time increases. The resulting brown color stored in a container. We did not observe any type of turbidity and precipitate during the storage time. For PtNPs, the aqueous solution of potassium tetrachloroplatinate (5.0 mL of 0.01 M) was added into the solution of aqueous extract. The reaction mixture was stirred for 1 h at room temperature,



**Scheme 1** Photo images (green and dry) *Artemisia herba-alba* plant and its water extract.

and solid PtNPs were obtained after the centrifugation. Seedless co-reduction method was used for the synthesis of Ag-Pt NPs (Zaheer et al., 2019). The solutions of metal salts precursors (silver nitrate and potassium tetrachloroplatinate) were added into the aqueous extract, and heated for 1 h at 40 °C. The solid Ag/Pt was collected by using centrifugation.

#### 2.4. Morphology determination

Surface morphology and elemental composition of Ag, Pt, and Ag-Pt NPs were determined by recording the SEM images and EDX of as-prepared NPs. The size and the size distribution were determined from the transmission electron microscope. Rigaku X-ray diffractometer equipped with a peltier-cooled solid state detector was used to determine the x-ray diffraction patterns (XRD). UV-visible spectra of an extract, Ag, Pt, and Ag/Pt NPs were measured on a Shimadzu UV-vis multi Spec-1501 spectrophotometer. The FT-IR spectra were recorded with Varian FTIR-640 spectrometer to establish the capping action of caffeic acid in-situ fabrication of Ag/Pt NPs. Shimadzu TOC-VCPN equipped with IR spectrometer for carbon dioxide quantification was used to the measurements of total organic carbon of decomposed MG.

#### 2.5. Degradation of MG dye

The dye degradation experiments were performed in 40 mL reactor. The  $K_2S_2O_8$  solution (16.0 mL of 0.01 mol/L) was added to the reactor, then the dye solution (5.0 mL of 0.01 mol/L), then the Ag-Pt (activator, 16 mg/L), and deionized water (19.0 mL) for dilution. The pH of the solution was adjusted with standard hydrochloric acid and sodium hydroxide. At a given time intervals, the sample aliquots were taken from the reactor and sodium azide (1.0 mL of 0.01) was added to quench the oxidation of dye (Lau et al., 2007). A calibration plot based on the Beer-Lambert's law (absorbance at 620 nm versus [MG]) was prepared at 620 nm by recording the absorbance to standard malachite green solution concentration. For the range of concentrations, a linear relationship between absorbance and concentration was obtained. The concentration of unreacted MG was calculated from the absorbance at 620 nm (wavelength maxima of MG). All measurements were performed at a room temperature (25 °C) unless otherwise stated. Several sets of batch experiments (such

as effects of dye concentration, pH, persulfate concentration, temperature and dosage of Ag/Pt NPs) were carried out to establish the role of each parameter in the dye degradation. Eq.(1) was used to determine the degradation percentage of malachite green.

$$\text{Percentage degradation} = \frac{(A_0 - A_t)}{A_0} \times 100 \quad (1)$$

The pseudo-first order rate equation was used for the calculation of degradation rate constant ( $k_{app}$ ) (Eq. (2) (Pouretedal and Keshavarz, 2010).

$$\ln \left( \frac{A_0}{A_t} \right) = k_{app} t \quad (2)$$

For the stability determination of the activator, Ag-Pt was separated from the reaction mixture by using centrifugation after each degradation experiment, washed with deionized water, ethanol several times, and then dried in oven at 60 °C for another kinetic runs under the similar experimental conditions.

### 3. Results and discussion

#### 3.1. UV-visible spectra of aqueous extract

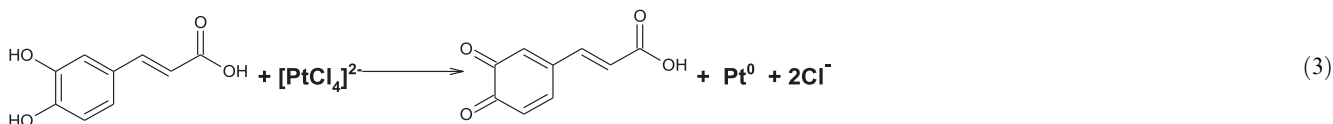
Fig. 1A shows the UV-visible spectra of the pale yellow color (extracted from the *Artemisia herba-alba*), which exhibits two absorption bands at 289 and 326 nm. These peaks attributed to the  $\pi \rightarrow \pi^*$  transitions of  $-\text{COOH}$  in the caffeic acid and an aromatic benzene moiety (Swislocka, 2013). The calibration plot was constructed between the absorbance at 326 nm and [caffeic acid] by using Beer-Lambert law. The molar extinction coefficient was determined from the calibration plot (Fig. 1B) and found to be 15,782 L/mol/cm. FT-IR spectroscopy proved to be a useful tool to get structural information of organic compounds. The FT-IR spectra of isolated and authentic caffeic acid were recorded for the comparison (Fig. 1C). The broad and intense peaks at 3440  $\text{cm}^{-1}$  and 3135  $\text{cm}^{-1}$  were ascribed to the  $-\text{OH}$  and carbon-carbon single bond stretching vibrations. The strong band at 1763  $\text{cm}^{-1}$  assigned to the stretching vibrations of carbonyl group of caffeic acid. For aromatic and carbon-carbon double bonds stretching vibrations, the peaks were observed at 1384  $\text{cm}^{-1}$ , 1269  $\text{cm}^{-1}$  and 1080  $\text{cm}^{-1}$  (Swislocka, 2013).

### 3.2. Preparation of metal NPs

UV-visible spectra of Ag and Pt NPs were recorded at different time intervals to establish the stability of NPs. Fig. 2A shows that the spectra of AgNPs has intense broad absorption band from 400 to 600 nm, which indicates the formation of AgNPs with mixed morphology (spherical, triangular, and truncated triangular). Inspection of Fig. 2A clearly indicates that the intensity of caffeic acid peaks decrease with time and new absorption peak was appeared. Table 1 shows the effects of different parameters ([metal ions], and [caffeic acid]) on the appearance, position of SPR band and stability of Ag NPs. In order to see the effect of storage time, optical images of AgNPs recorded as a function of time (Scheme 2). These visual observations can be ascribed due to the formation of colored silver sols during the redox reaction between silver ions and caffeic acid.

The resulting silver sols became perfect transparent and no precipitate was observed during the observations, indicates that the AgNPs was capped with caffeic acid, which has strong tendency to formed complex with metal ions (Scheme 3) (Cornard et al., 2006).

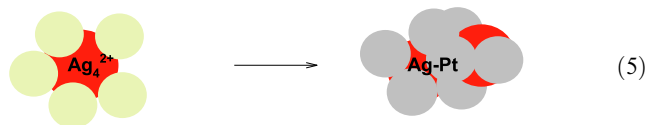
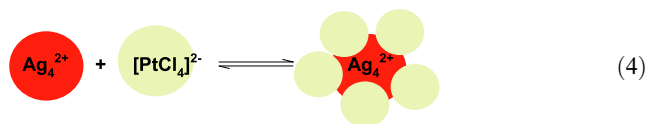
Fig. 2B shows the time-resolve UV-visible spectra of Pt NPs. The absorption intensity of caffeic acid at 326 nm decreases after the addition of an aqueous solution of  $[\text{PtCl}_4]^{2-}$ , which suggests formation of  $\text{Pt}^0$  by the reduction of  $[\text{PtCl}_4]^{2-}$  with caffeic acid (Eq. (3)). UV-visible spectra of metallic  $\text{Pt}^0$  was featureless in the entire visible region (Table 1). Our results are in accordance to the suggestion of Creighton and Eadon regarding the UV-visible spectra of Pt NPs (Creighton and Eadon, 1991).



Optical images of caffeic acid,  $[\text{PtCl}_4]^{2-}$ , and Pt NPs are given in Scheme 4.

Ag-Pt bimetallic NPs were fabricated using seedless co-reduction method under various concentration of caffeic acid and metal ions precursor (Table 1). In a typical experiment, an equimolar solutions of silver nitrate and  $[\text{PtCl}_4]^{2-}$  (2.0 mM) were added into the conical flask containing the 0.11 mM caffeic acid at 22 °C. The progress of the redox reaction was monitored by recording the UV-visible spectra of Ag/Pt NPs with time. Surprisingly, no SPR band was appeared in the vicinity of 400 to 600 nm, which is the characteristic of mono-metallic AgNPs, indicating the formation of Ag-Pt NPs. Optical images of reaction mixture containing silver nitrate,  $[\text{PtCl}_4]^{2-}$ , and caffeic acid were recorded. The colorless solution became pale yellow to gray-orange, which indicates the formation of Ag-Pt NPs (Scheme 5).

In a seedless co-reduction of  $\text{Ag}^+$  and  $[\text{PtCl}_4]^{2-}$  by caffeic acid, there is a competition between the metal ions to gains electrons from the reducing agent (Goia and Matijevic, 1998; Cheng et al., 2012). The  $\text{Ag}^+$  ions were first reduced by caffeic acid to generate Ag NPs, because  $\text{Ag}^+$  ions had a higher reducing potential (reduction potential ( $E^0$ ) = 0.799 V for  $\text{Ag}^+/\text{Ag}^0$ ) than  $[\text{PtCl}_4]^{2-}$  ions (reduction potential ( $E^0$ ) = 0.755 for  $[\text{PtCl}_4]^{2-}/\text{Pt}^0$ ). Consequently, the  $[\text{PtCl}_4]^{2-}$  ions would be reduced on the surface of the Ag NPs under potential deposition (Liu et al., 2014). Inspection of Fig. 3 clearly suggests that the color and position of SPR band of the resulting Ag-Pt NPs were dominated by the outer surface of the Pt NPs. Thus we may state confidently that the Ag-Pt NPs were formed during the seedless co-reduction of silver and  $[\text{PtCl}_4]^{2-}$  ions by caffeic acid (Eqs. (4) and (5) (Liu et al., 2014).



$[\text{PtCl}_4]^{2-}$  ions was deposited on to the positive surface of AgNPs via electrostatic and van der Waals interactions (Eq. (4)). In the next step,  $[\text{PtCl}_4]^{2-}$  ions were reduced under potential deposition, and Ag-Pt NPs were formed (Eq. (5)).

### 3.3. Morphology of NPs

Surface morphology and elemental composition of Ag, Pt, and Ag-Pt NPs were determined by recording the SEM images and EDX of as-prepared NPs. Fig. 2A and 2B (in set) shows the SEM images with UV-visible spectra of Ag, and Pt NPs, respectively. The particles are spherical in shape and aggregated to each other. Ag/Pt NPs are also spherical in shape and formed a layered sheet like structure due to the deposition of one metal onto the other (Fig. 4, indicated by red circle). Such type of morphology was not observed in case of mono-metallic Ag and Pt NPs. TEM image of AgNPs indicates the formation spherical, triangular, irregular, and poly-dispersed NPs (Fig. 2A TEM image), while the PtNPs are interconnected to each other and formed beautiful chain of metallic Pt (Fig. 2B, TEM image). For Ag-Pt NPs, small granules

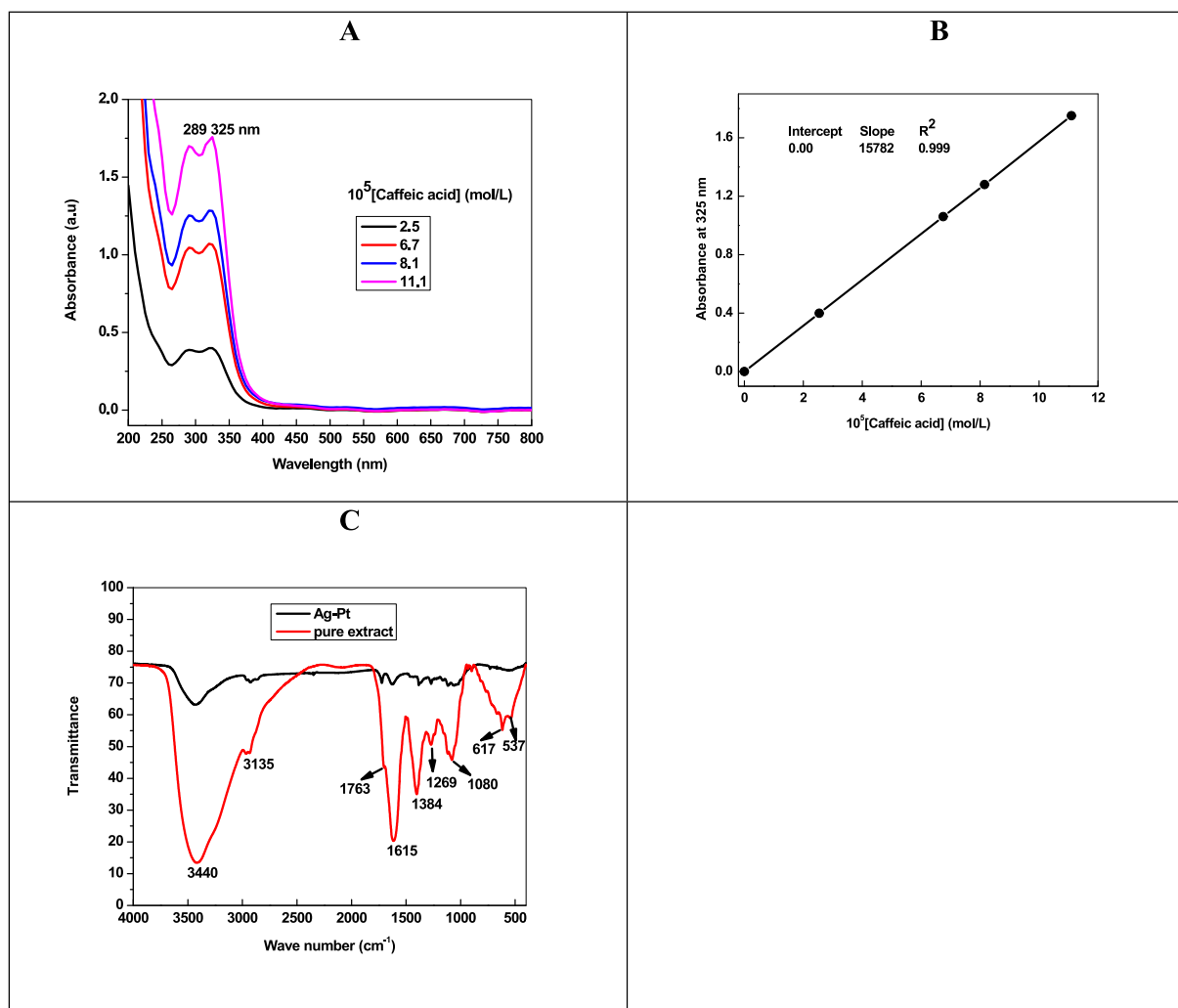


**Fig. 1** UV-visible spectra of (A), Beer-Lambert plot (B), and FT-IR spectra of caffeic acid extracted from *Artemisia herba-alba*.

adsorbed onto the surface of each other, and leads to the formation of large size NPs. Inspection of Fig. 4 TEM image suggests that the grains of metals formed a flower like morphology of metallic  $\text{Ag}^0$  and  $\text{Pt}^0$  at 20 nm scale. High resolution TEM image clearly indicates the presence of both metals in Ag-Pt NPs (Fig. 4). EDX spectra and percentage of elements present in all samples are given in Fig. 5, which shows the presence of Ag, Pt, and Ag-Pt along with the carbon and oxygen. The XRD patterns of AgNPs, PtNPs and Ag-PtNPs are given in Fig. 6A, which clearly suggests the formation of pure Ag, Pt, and Ag-Pt NPs. For AgNPs, the diffraction peaks observed at  $2\theta = 42.2$  (111),  $54.6$  (200),  $63.5$  (220), and  $77.4^\circ$  (311) planes of  $\text{Ag}^0$  (Fig. 6A). For Pt NPs, three peaks located as  $2\theta = 39.8^\circ$ ,  $46.7^\circ$ , and  $67.6^\circ$ , which are the characteristic of the (111), (200), and (220) diffraction planes of the crystalline  $\text{Pt}^0$  NPs, respectively, (JCPDS card no. 04-0802). For Ag-Pt NPs, all diffraction peaks are merged together, which indicates the formation of Ag-Pt NPs (Fig. 6A). The average crystallite size of Ag-Pt NPs was determined with Debye-Scherrer equation ( $D = C\lambda / \beta \cos\theta$ , where  $D =$  size in  $\text{\AA}$ ,  $C =$  shape factor constant equal to 0.94,  $\lambda = 1.5418 \text{ \AA}$ ,  $\beta =$  full-width at half-

maximum in radians, and  $\theta =$  Bragg's diffraction angle for the peak in degrees). The size of Ag-Pt was found to be 20 nm.

From the UV-visible spectrum of Ag-Pt NPs, the optical band gap ( $E_g$ ) was calculated with (Eq. (6)).

$$\left(\alpha \frac{1240}{\lambda}\right)^2 = \frac{1240}{\lambda} - E_g \quad (6)$$

where  $\alpha$ ,  $\lambda$ , and  $E_g$  are the absorption value in the UV-visible spectrum, detection wavelength, and optical band gap, respectively. Fig. 6B was constructed between the  $(\alpha 1240 / \lambda)^2$  and  $1240 / \lambda$  as Y- and X-axis, respectively. The  $E_g = 2.72 \text{ eV}$  was estimated by extrapolating a straight line to the  $(\alpha 1240 / \lambda)^2 = 0$  axis in the plot of  $(\alpha 1240 / \lambda)^2$ .

In order to determine the oxidation states of Ag and Pt in the Ag-Pt NPs, XPS analyses were carried out. The XPS spectra for survey, Ag 4d, Pt 4f, O 1s, and C 1s are shown in Fig. 7A. The overall spectrum consists the main characteristic peaks appeared at the binding energy of Pt 4f at 75.98 eV, O 1s at 533.68 eV, Ag 3d at 369.17 eV, and C 1s at 286.15 eV. As displayed, the Ag 3d spectrum can be deconvoluted into two doublet at 368.23 and 374.18 eV (spin-orbit

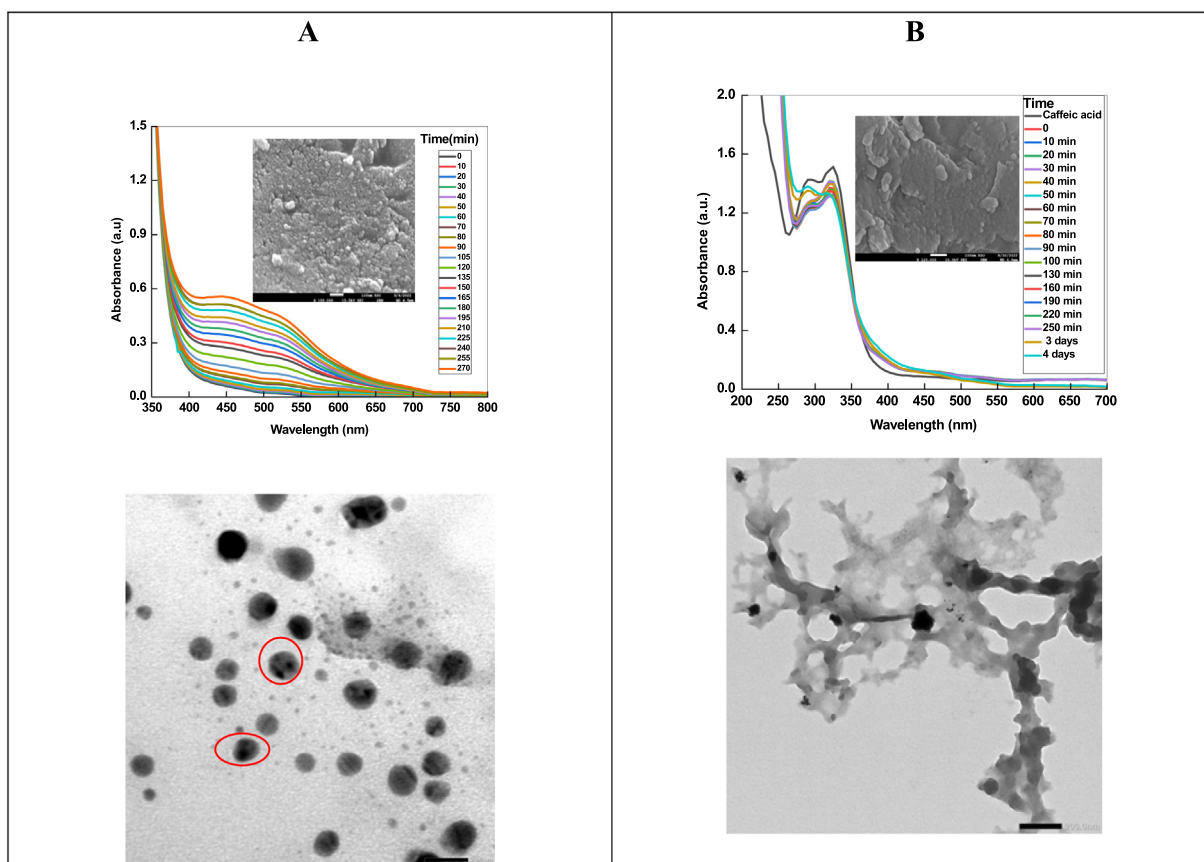


**Fig. 2** Time resolved spectra Ag NPs (A) and Pt NPs (B) along with TEM images. In set- SEM images for both NPs.

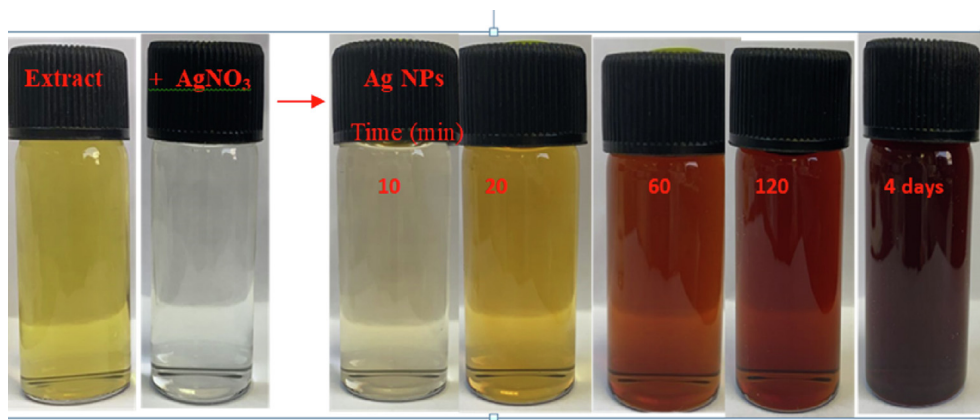
**Table 1** The position of SPR band and stability of Ag, Pt, and Ag-Pt NPs.

[Caffeic acid] (mM)	[Metal ions] (mM)	Optical properties of NPs
0.15	Ag <sup>+</sup> 1.0	Pale yellow, stable, SPR band = 400–600 nm, Ag <sup>0</sup>
0.15	Ag <sup>+</sup> 2.0	Yellow, stable, SPR band = 400–600 nm, Ag <sup>0</sup>
0.25	Ag <sup>+</sup> 2.0	Brown, stable, SPR band = 400–600 nm, Ag <sup>0</sup>
0.40	Ag <sup>+</sup> 2.0	Brown red, stable, SPR band = 400–600 nm, Ag <sup>0</sup>
0.15	PtCl <sub>4</sub> <sup>2-</sup> 1.0	Pale yellow, stable, no SPR band, Pt <sup>0</sup>
0.15	PtCl <sub>4</sub> <sup>2-</sup> 2.0	Pale gray, stable, no SPR band, Pt <sup>0</sup>
0.15	PtCl <sub>4</sub> <sup>2-</sup> 3.0	Gray, stable, no SPR band, Pt <sup>0</sup>
0.25	PtCl <sub>4</sub> <sup>2-</sup> 2.0	Gray, stable, no SPR band, Pt <sup>0</sup>
0.40	PtCl <sub>4</sub> <sup>2-</sup> 2.0	Gray, stable, no SPR band, Pt <sup>0</sup>
0.15	Ag <sup>+</sup> + PtCl <sub>4</sub> <sup>2-</sup> 1.0	Pale yellow, stable, no SPR band, Ag-Pt
0.15	Ag <sup>+</sup> + PtCl <sub>4</sub> <sup>2-</sup> 2.0	Yellowish gray, stable, no SPR band, Ag-Pt
0.15	Ag <sup>+</sup> + PtCl <sub>4</sub> <sup>2-</sup> 3.0	Dirty gray, stable, no SPR band, Ag-Pt
0.25	Ag <sup>+</sup> + PtCl <sub>4</sub> <sup>2-</sup> 2.0	Dirty gray, stable, no SPR band, Ag-Pt
0.40	Ag <sup>+</sup> + PtCl <sub>4</sub> <sup>2-</sup> 2.0	Dirty gray, stable, no SPR band, Ag-Pt

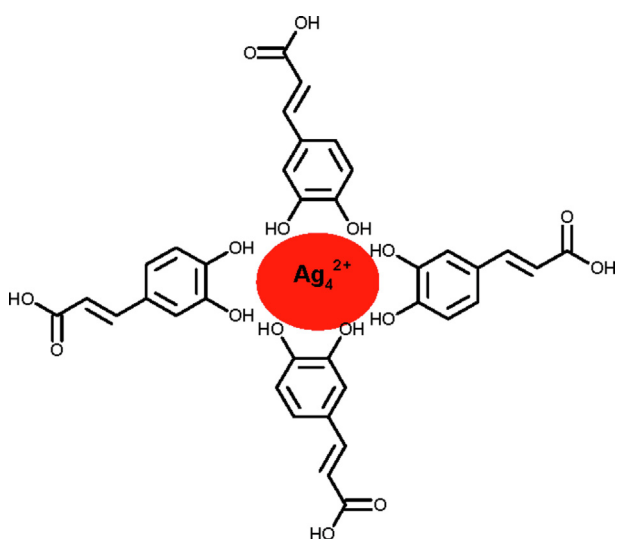
separation = 6.0 eV) corresponds to 3d<sub>5/2</sub> and Ag 3d<sub>3/2</sub>, respectively, for metallic Ag state (Fig. 7B). The high resolution spectrum was recorded in the Pt 4f (4f<sub>5/2</sub> and 4f<sub>7/2</sub>) region. The doublet peaks at 80.1 eV and 87.67 eV with spin-orbit separation of 3.67 eV, which are ascribed to the binding energies of metallic Pt 4f<sub>7/2</sub> and Pt 4f<sub>5/2</sub>, respectively (Fig. 7C). The high resolution XPS peak of C 1s, and O 1s, respectively, at 286.23 eV, and 533.68 eV were observed (Fig. 7D and 7E).

### 3.4. Degradation of MG

UV-visible spectra of MG exhibits three absorption band at 314, 424 and 620 nm in water (Kitching et al., 2014). Out of these, the absorbance was maximum at 620 nm. Therefore, degradation of green color of dye was monitored with Ag-Pt as activator for K<sub>2</sub>S<sub>2</sub>O<sub>8</sub> as a model dye by advanced oxidation processes (Scheme 6).



**Scheme 2** Visual observation to the formation of AgNPs by silver ions-caffeic acid redox reaction at room temperature.

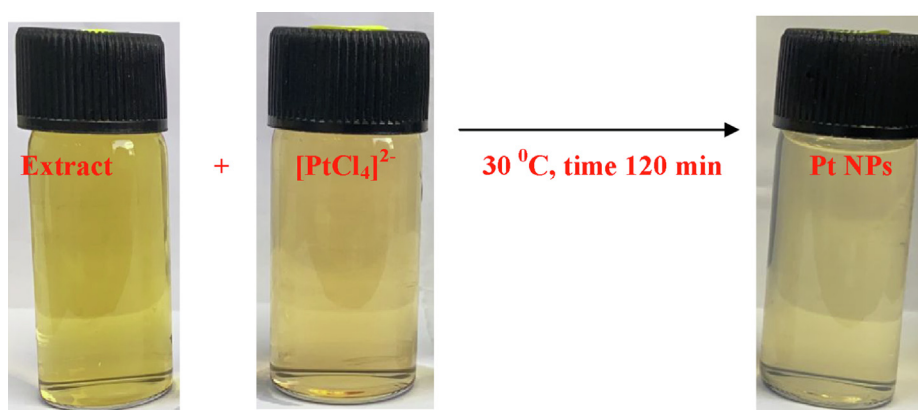


**Scheme 3** Capping action of caffeic acid with AgNPs.

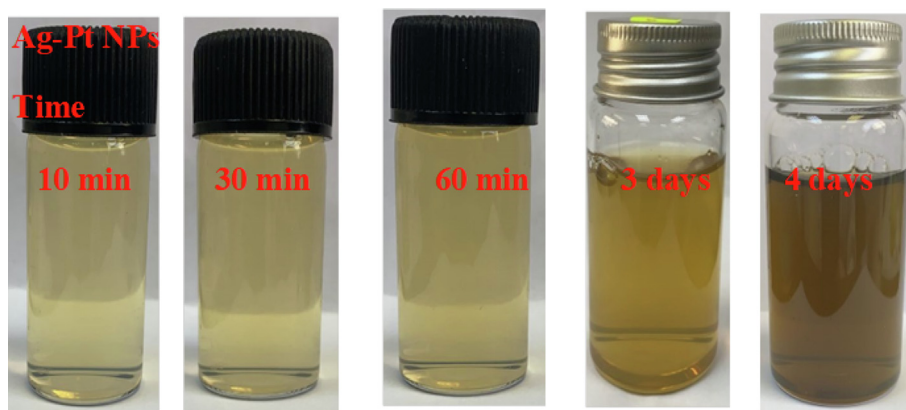
In order to see insight into the role of Ag-Pt and  $K_2S_2O_8$  on the degradation of MG, a series of experiments was performed with various conditions for example: (1) MG + Ag-Pt NPs, (2) MG +  $K_2S_2O_8$  and (3) MG + Ag-Pt +  $K_2S_2O_8$  (Table 2). It

was observed that the degradation of dye was not occurred with Ag-Pt NPs and/or  $K_2S_2O_8$ . The optical images demonstrate that no significant MG oxidation takes place with Ag-Pt and  $K_2S_2O_8$ . As shown in Fig. 8, when small amount of  $K_2S_2O_8$  (4.0 mM) was added to the reaction mixture of MG and Ag-Pt, the absorbance at 620 nm decreases with reaction time, and green color reaction solution became colorless within 50 min. The spectral changes indicate that the peroxide bond of  $K_2S_2O_8$  activated by Ag-Pt NPs, and reactive radical species generated, which decolorized and mineralized the MG. These observations are in good agreement to the results of other investigators (Gokulakrishnan et al, 2012; Lu et al. 2020) regarding the heterogeneous oxidation of MG with activated persulfate by different methods. The primary intermediate(s) and degradation by products of dye depends on the nature of the reactive radical species as well as method of the oxidation (chemical and biochemical) (Saqib and Muneer, 2003; Azmi and Sani, 1998). Benzophenone derivatives, benzaldehyde, benzene, nitrobenzene, p-aminobenzoic acid, aniline, and others were identified as the intermediate(s) degradation products of MG under different experimental conditions (Berberidou et al. 2007; Gokulakrishnan et al, 2012; Lu et al. 2020; Saqib and Muneer, 2003).

The effects of Ag-Pt concentration (=8.0 mg to 16.0 mg) on MG decolorization were investigated at fixed [MG] = 1.2 5 mM,  $[S_2O_8^{2-}] = 4.0$  mM, and temperature = 30 °C, and



**Scheme 4** Optical images of Pt NPs after 120 min at 30 °C.



**Scheme 5** Optical images of Ag-Pt NPs formation as a function of time.

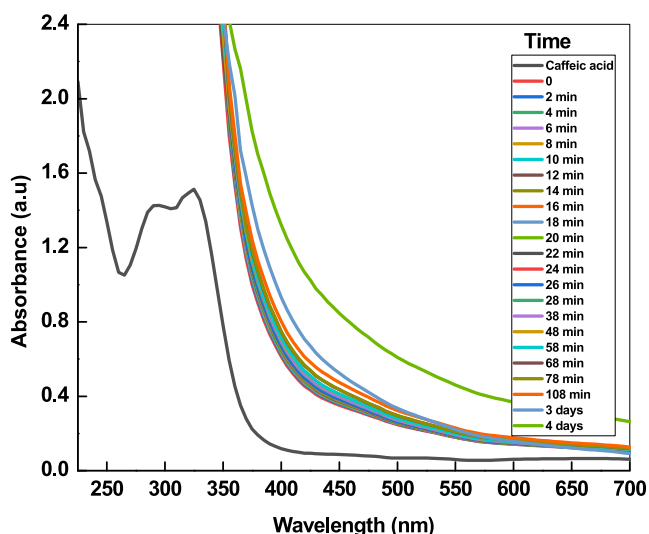


**Fig. 3** Time resolved spectra of Ag-Pt NPs.

the results obtained are presented in Fig. 9A. The Mg degradation % was significantly increased over the concentration of Ag-Pt dosage. The degradation efficiency was also increases with the amount of the activator (Table 2). The 94.2% dye was decomposed at 16 mg of Ag-Pt after 50 min of reaction time. The effects of MG concentration were investigated at different initial concentrations in the range of 0.75 to 2.5 mM at fixed amount of activator (16 mg/L), pH (7.0) and temperature (25 °C). As shown in Fig. 9B, the rate of dye degradation decreases with increasing initial concentration of MG, which was also reported in other metal NPs activated persulfate oxidation of toxic water contaminants (Zhang et al., 2020; Liang et al., 2013; Hu et al., 2019). The degradation of MG was also investigated over the pH range of 4 to 10 with fixed concentration of dye (1.25 mM), amount of Ag-Pt (16 mg),  $K_2S_2O_8$  (4.0 mM) at 30 °C. The following sequence in the degradation of MG in the  $S_2O_8^{2-}/Ag-Pt$  combined system at different initial pH was observed: pH 7 > pH 4 > pH 8 > pH 13 > pH 10 (Fig. 9C). The neutral aqueous medium was the optimal initial pH for the dye degradation in the  $S_2O_8^{2-}/Ag-Pt$ . At low and high pH, the decrease in the oxidation capacity of  $S_2O_8^{2-}$  has

been attributed to the involvement of  $SO_4^{\bullet}$  in other reactions (Liang et al., 2013; Al-Shehri et al., 2021).

The complete degradation of MG was observed at lower  $S_2O_8^{2-}$  concentration ( $\geq 1.0$  mM). The rate of degradation increased with increasing  $S_2O_8^{2-}$  from 1.0 to 6.0 mM. On further increasing the  $S_2O_8^{2-}$  concentration from 7.0 mM, decreased in the MG decolorization (Fig. 9D). The degradation rate increases and decreases with the  $[S_2O_8^{2-}]$ , which indicates the participation of  $S_2O_8^{2-}$  in  $SO_4^{\bullet}$  generator ( $S_2O_8^{2-} + Heat/metal\ NPs \rightarrow 2SO_4^{\bullet}$ ) and  $SO_4^{\bullet}$  scavenger ( $2SO_4^{\bullet} \rightarrow S_2O_8^{2-}$ ). For  $[S_2O_8^{2-}] = 4.0$  mM, the  $k_{app}$  and % degradation were found to be  $0.055\ min^{-1}$  and 94.2 %, respectively. The efficiency of % degradation depends on the persulfate activator (metal ions, metal NPs, temperature, UV light), structure of dye, and pH (Behnajady et al., 2008; Colonna et al., 1999; Deng et al., 2013).

The  $K_2S_2O_8$  was activated by heat and generates reactive radical species. In order to study to effect of temperature on the cleavage of peroxide bond of  $K_2S_2O_8$  and degradation of malachite green, the effect of temperature was carried out at 25, 35, 45 and 55 °C. The rate of degradation increased from  $0.055\ min^{-1}$  to  $0.162\ min^{-1}$  as a consequence of increasing the temperature from 25 to 55 °C (Table 2). This is because of higher temperature increased the rate of decomposition of peroxide linkage of  $K_2S_2O_8$ , thus increasing the rate of generation of reactive radical species such as  $SO_4^{\bullet}$  and  $HO^{\bullet}$ , which in turn, enhanced the degradation of malachite green. The Arrhenius equation ( $\ln k_{app} = \ln A - E_a/RT$ , where  $k_{app}$  = rate constant,  $E_a$  = activation energy,  $R$  = gas constant, and  $T$  = temperature in Kelvin) was used for the calculation of activation energy. From the slope of the  $\ln k_{app}$  versus  $1/T$ , the activation energy is found to be  $29.7\ kJ\ mol^{-1}$  with  $R^2 = 0.996$ . The lower value of activation energy suggests that the two effects, namely, temperature as well as Ag-Pt NPs operates simultaneously and activates the cleavage of peroxide bond (Ahn et al., 2019). Table 3 shows that the degradation efficiency was found to be 0.0% 55.2%, 94.2%, respectively, for Pt, Ag, and Ag-Pt NPs in 30, 50, and 50 min in presence of 4.0 mM  $S_2O_8^{2-}$ . The best  $S_2O_8^{2-}$  activator for MG oxidation was found to be Ag-Pt NPs [ $Ag-Pt > Ag^0 > Pt^0$ ], which might be due to the synergistic effect of both metals. The bimetallic system was more promising than monometallic for the heterogeneous activation of  $S_2O_8^{2-}$  (Al-Shamsi, et al., 2013). The second metal serves as an additional electron donor, increase the surface area of

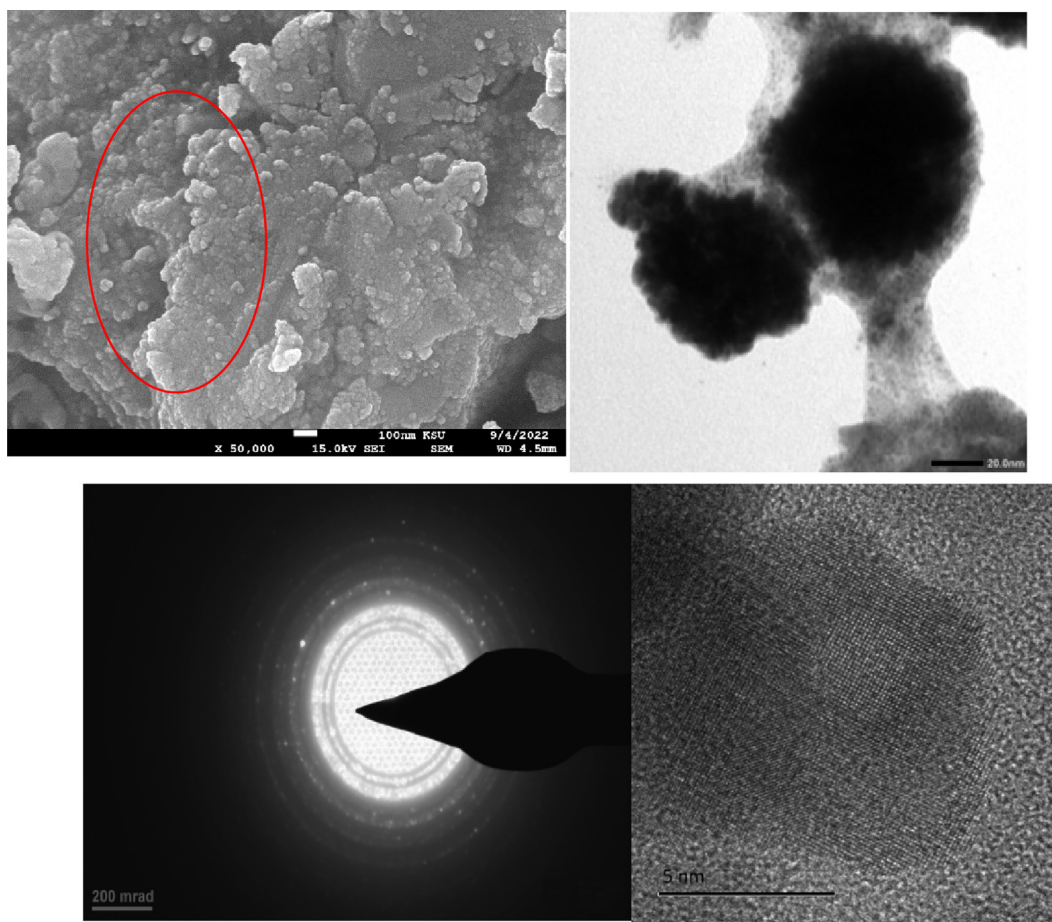


**Fig. 4** SEM and TEM (high resolution, and corresponding lattices) images of Ag-Pt NPs.

monometallic NPs by depositing a non-uniform layer on the surface of the NPs, and form a galvanic corrosion system on the surface of NPs, which enhances the catalytic ability of the NPs (Zhang, et al., 1998).

The degradation efficiency percentage was evaluated from Eq.(1) and found to be increased with reaction time at fixed concentrations of other parameters. The 94.2% MG was degraded in 50 min (Fig. 10A), and green color of dye disappeared completely after 90 min (Fig. 8 optical images). Fig. 8 shows that the some organic intermediate(s) are present in the residual solution for longer reaction time. This indicates that a lower mineralization efficiency is attained as a result of the existence of small toxic oxidation products of the used dye. It has been established that the decolorization and mineralization (formation of CO<sub>2</sub> and water) were the two different steps of the complete dye decomposition (Aleboye et al., 2008; Lu et al., 2020; Huang et al., 2021). Fig. 10B shows the decay of absorbance at 320 nm (related to the absorbance of poly aromatic rings), and 620 nm (related to the destruction of conjugated system of dye) for the mineralization and decolorization of dye, respectively (Behnajady et al., 2008). At 620 nm, the absorbance decreases from 0.34 to 0.036 (94.2% degradation) after 50 min of reaction time and remained unchanged approximately after it, which might be related to the destruction of conjugated system of MG green as well as N-demethylation processes. On the other hand, absorbance

decreases from 0.22 to 0.016 (60 % degradation) at 320 nm after the same reaction time, which can be ascribed due to the destruction of benzene moieties of dye. The mineralization efficiency was monitored by recording the change in the total organic content of MG. The mineralization efficiency was evaluated with the following relation (Eq. (7)).

$$\text{Mineralization}(\%) = \left( \frac{[\text{TOC}]_0 - [\text{TOC}]}{[\text{TOC}]_0} \right) \times 100 \quad (7)$$

where [TOC]<sub>0</sub> = TOC at initial time, and [TOC] = TOC concentrations at time t. Fig. 10C shows that the mineralization process has an induction period (decolorization period). The 8.0% of TOC degradation was observed in solution for both [MG]<sub>0</sub> / [S<sub>2</sub>O<sub>8</sub><sup>2-</sup>]<sub>0</sub> during the first 20, 40, and 60 min. Fig. 10D shows the TOC ratio ([TOC] / [TOC]<sub>0</sub>) in aqueous MG solutions at different time for different [MG/S<sub>2</sub>O<sub>8</sub><sup>2-</sup>]. The mineralization process is lower than those for the decolorization, indicates that the destruction of conjugated system due to azo bond is the first step of MG decomposition (Scheme 7). The generated HO• reacts with S<sub>2</sub>O<sub>8</sub><sup>2-</sup> and converted into HO<sup>-</sup> and corresponding radical at all pH values (HO• + S<sub>2</sub>O<sub>8</sub><sup>2-</sup> → HO<sup>-</sup> + S<sub>2</sub>O<sub>8</sub><sup>•-</sup>, k = 1.2 × 10<sup>7</sup> mol<sup>-1</sup> dm<sup>3</sup> s<sup>-1</sup>) (Liang and Su, 2009). Fig. 10D clearly suggests that the end products of degraded MG does not completely mineralize into CO<sub>2</sub> and H<sub>2</sub>O for extended reaction time (Aleboye et al., 2008).

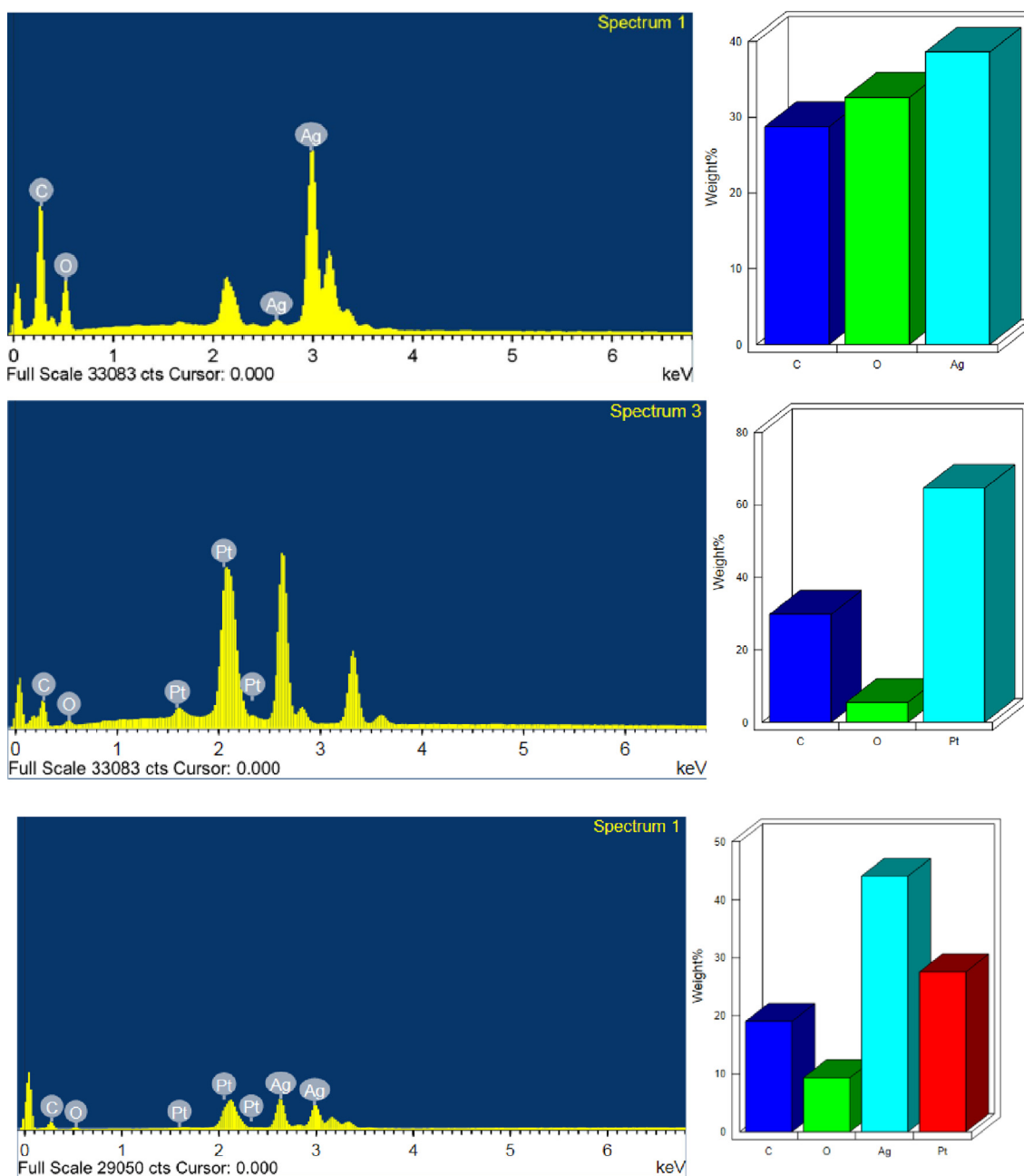


Fig. 5 EDX spectra of Ag (A), Pt (B), and Ag-Pt NPs (C).

In Scheme 7 represents the decolorization of MG into colorless MG intermediate due to the addition reaction between  $\text{HO}^-$  and MG. For the decolorization of dye, the first step is the addition of  $\text{HO}^-$  on to the MG, which diminished the chromophoric structure of MG (Huang, et al., 2021). The 12 and 20 degradation intermediates of MG with  $\text{Fe}_3\text{O}_4/\text{GAs} + \text{S}_2\text{O}_8^{2-} + \text{light}$  (Lu et al. 2020) and  $\text{CuFe}_2\text{O}_4@ \text{biochar}/\text{S}_2\text{O}_8^{2-}$  (Huang et al., 2021) systems were detected by using LC-MS and UPLC-MS, respectively. These investigators suggested that the MG was completely degraded via two possible routes, and eventually mineralized into  $\text{CO}_2$  and  $\text{H}_2\text{O}$ . On the basis of UPLC-MS data, Huang et al. also proposed the similar mechanism for the degradation of MG, and suggests that the

addition of  $\text{HO}^-$  with MG is the first step (Huang, et al., 2021). The intermediate was slowly mineralized into the  $\text{CO}_2$  and  $\text{H}_2\text{O}$  by the generated radical species (Gokulakrishnan et al., 2012; Xu and Le, 2010; Li et al., 2015).

### 3.5. Ag-Pt as activator of $\text{K}_2\text{S}_2\text{O}_8$

Fig. 7 optical images show that the green color of malachite green became colorless after the treatment with  $\text{S}_2\text{O}_8^{2-}/\text{Ag-Pt}$  system. The color and suspension of Ag-Pt NPs was not visualized after the degradation of dye, indicating the metallic silver and platinum were oxidized into the corresponding metal ions ( $\text{Ag}^+$  and  $\text{Pt}^+$ ). The generated  $\text{HO}^\bullet$  species, formed after

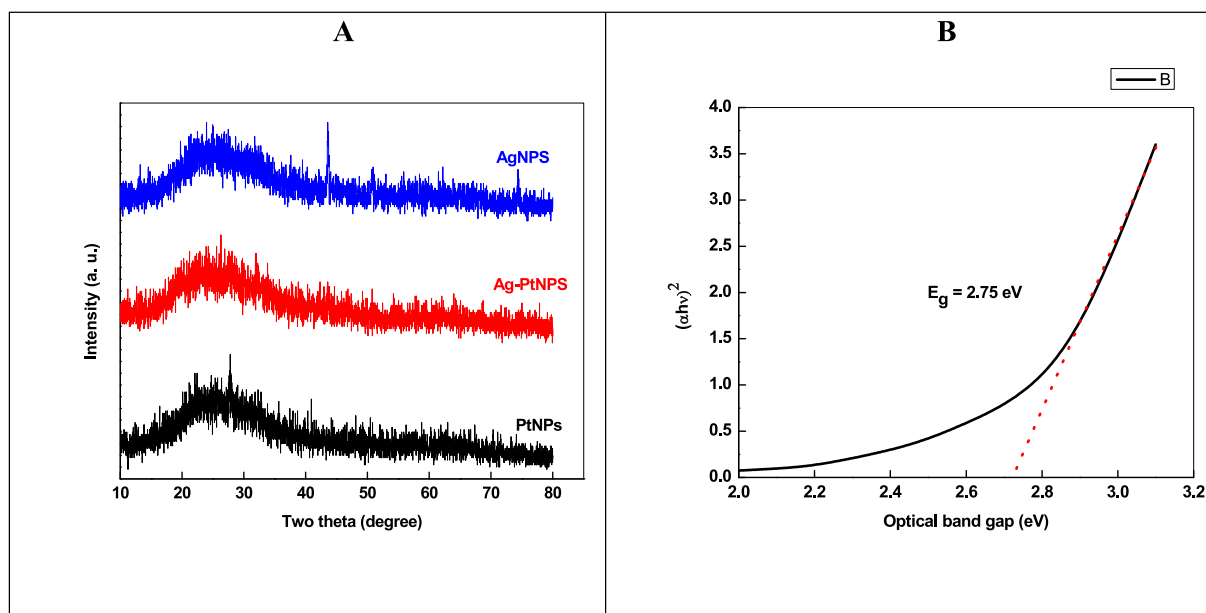
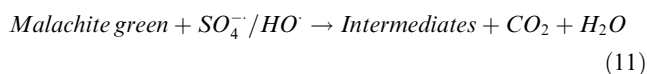
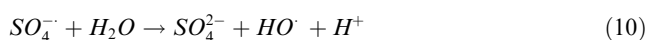
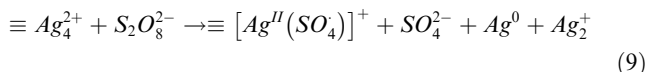
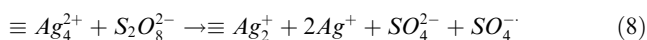


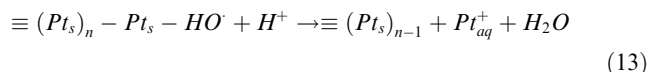
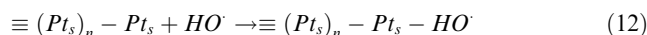
Fig. 6 XRD (A), and optical band gap plot (B) of Ag-Pt NPs.

the activation of  $S_2O_8^{2-}$  by Ag-Pt, may initiate a series of radical chain reactions. The possible degradation mechanism of MG with  $S_2O_8^{2-}$ /Ag-Pt might occur as Eqs. (8) to (11) listed below (Anipsitakis and Dionysiou, 2004).



The  $Ag^+$  ions onto the surface of  $Ag^0$  acted a heterogeneous  $S_2O_8^{2-}$  activator and generates  $SO_4^{\cdot-}$  through the cleavage of peroxide bond of  $S_2O_8^{2-}$ . First,  $Ag^+$  on the surface of Ag-Pt will activate  $S_2O_8^{2-}$  to generate  $SO_4^{\cdot-}$  and transfer the  $Ag^+$  ions to higher valence state (Eq. (8)). AgNPs also formed cage complex with  $S_2O_8^{2-}$  (Eq.9). The  $HO^{\cdot}$  radicals were generated in solution after the reaction of  $SO_4^{\cdot-}$  with water (Eq. (10)). Both radicals ( $HO^{\cdot}$  and  $SO_4^{\cdot-}$ ) possesses strong oxidizing activity and oxidized target organic water contaminants to  $CO_2$  and  $H_2O$  (Eq. (11)). The presence of Pt NPs accelerated the generation of  $SO_4^{\cdot-}$  radicals due to their strong galvanic metal displacement cell reaction with zero valent silver NPs, in which Pt NPs and Ag NPs acts as catalyst (cathode), and an electron donor (anode), respectively. As a result, the  $Pt^0$  helps to increase the ability of AgNPs. Ahn et al. suggested that the

surface metal such as Pt and Au were the most appealing activator to generate  $SO_4^{\cdot-}$  radicals in the M/ $Al_2O_3$  composite (Ahn et al., 2019). The reason behind the role of metal type is unknown, while the efficient activation by Pt in Ag-Pt might be related to the intrinsic surface catalytic property of these metals (Eqs. (12) to (14)).



The  $Pt^0$  and  $Ag^0$  were oxidized to produce corresponding ions by hydrogen peroxide, and air + ascorbic acid, respectively, in an aqueous solution through oxidation etching process (Okamoto, et al., 2012; Wang, et al., 2013). The oxidative dissolution of NPs could be due to the direct redox reaction with the reactive oxygen radical species and/or natural organic materials in aquatic system (Wang, et al., 2016).  $S_2O_8^{2-}$  activation by Ag-Pt NPs involves the oxidation of both metals ( $Ag^0$  and  $Pt^0$ ) and subsequent their aqueous dissolution (Aljadaani, et al., 2021). Thus the generation of  $SO_4^{\cdot-}$  by the decomposition of  $S_2O_8^{2-}$  with transition metals and/or metal NPs is not truly a catalytic process. Ag-Pt NPs serves as a sacrificial electron donor. On the basis of observed results and pervious existing literature, Scheme 8 mechanism was proposed for the activation and degradation of  $S_2O_8^{2-}$  and MG in Ag-Pt/ $S_2O_8^{2-}$  system (Liang, et al., 2017; Lu, et al., 2020; Huang, et al., 2021).

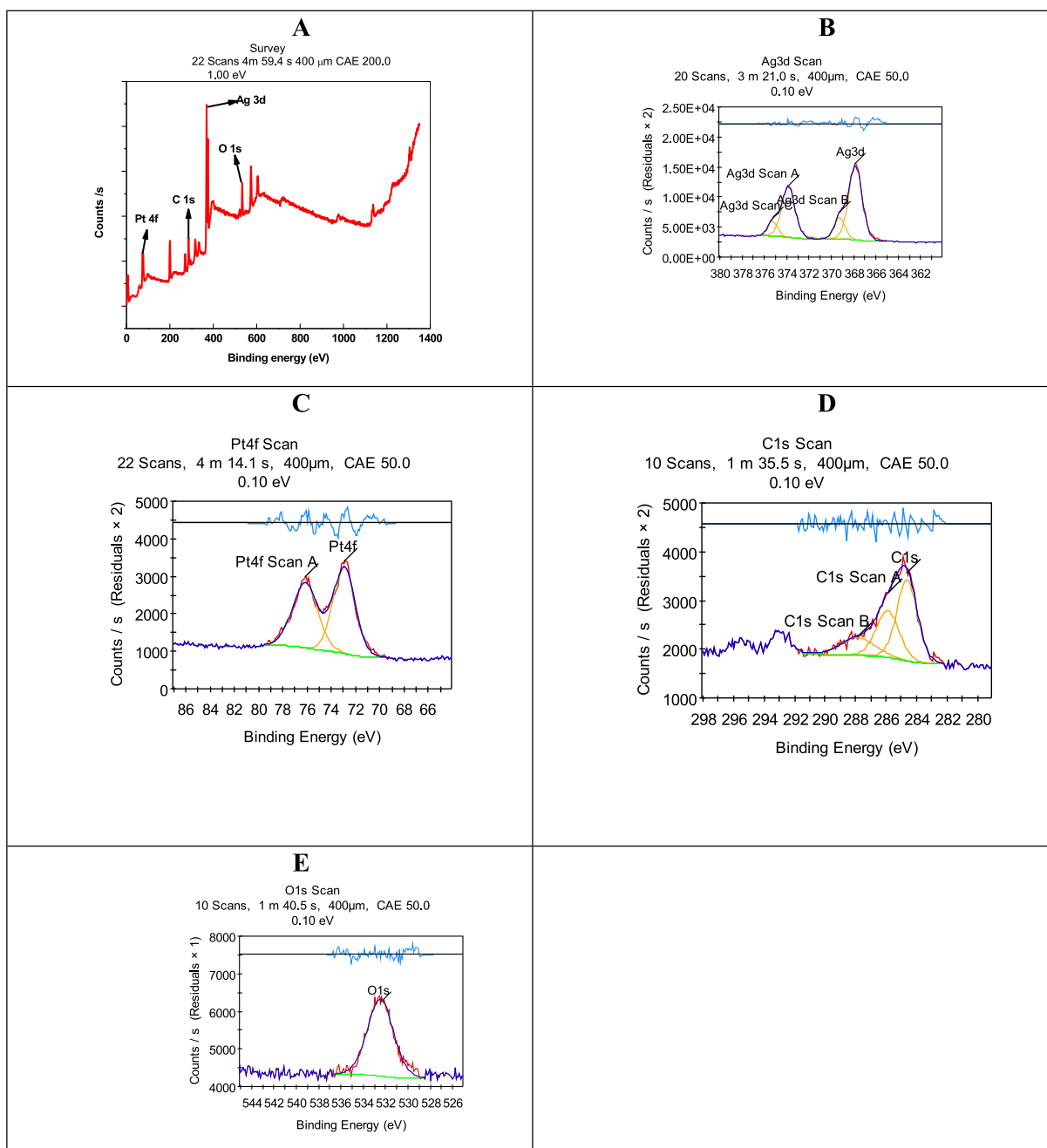
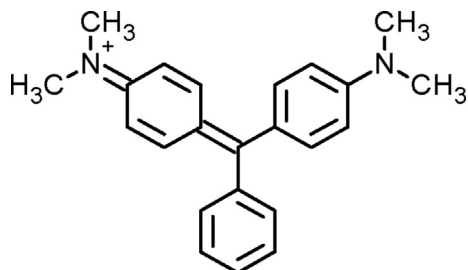


Fig. 7 XPS of Ag-Pt NPs.



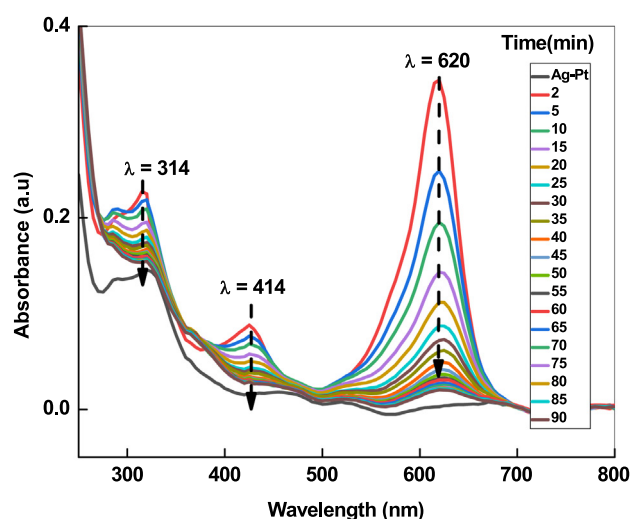
Scheme 6 Structure of MG.

### 3.6. Scavenger test and reusability

It has been established that the  $\text{SO}_4^{\bullet-}$  and  $\text{HO}^{\bullet}$  were the two main reactive radical species produced by  $\text{S}_2\text{O}_8^{2-}$  decomposition (Gu et al., 2018; Lu et al., 2020). Quenching tests were performed with ethanol, tertiary butanol (TBA), and potassium iodide to quench both  $\text{SO}_4^{\bullet-}$  and  $\text{HO}^{\bullet}$ , only  $\text{HO}^{\bullet}$ , and both  $\text{HO}^{\bullet}$  and  $\text{SO}_4^{\bullet-}$ , respectively. Fig. 11A displaced the effect of different quenchers on the oxidation of MG. The degradation efficiency was dropped 6.2% after adding 10 mM ethanol, indicating that ethanol quench the both  $\text{HO}^{\bullet}$  and  $\text{SO}_4^{\bullet-}$  radi-

**Table 2** Effects of Ag-Pt, MG,  $S_2O_8^{2-}$ , pH, and temperature on the degradation of malachite green.

Ag-Pt (mg)	[MG] (mM)	[ $K_2S_2O_8$ ] (mM)	pH	Temperature ( $^{\circ}C$ )	$k_{app}$ ( $min^{-1}$ )	$R^2$
6.0	1.25	4.0	3.0	25	0.016	0.996
10.0	1.25	4.0	3.0	25	0.024	0.996
12.0	1.25	4.0	3.0	25	0.038	0.992
16.0	1.25	4.0	3.0	25	0.055	0.994
16.0	0.07	4.0	3.0	25	0.092	0.994
16.0	1.0	4.0	3.0	25	0.081	0.991
16.0	2.0	4.0	3.0	25	0.036	0.993
16.0	2.5	4.0	3.0	25	0.012	0.995
16.0	1.25	4.0	4.0	25	0.078	0.995
16.0	1.25	4.0	7.0	25	0.095	0.997
16.0	1.25	4.0	8.0	25	0.062	0.998
16.0	1.25	4.0	10.0	25	0.032	0.992
16.0	1.25	1.0	3.0	25	0.022	0.996
16.0	1.25	6.0	3.0	25	0.082	0.998
16.0	1.25	7.0	3.0	25	0.043	0.992
16.0	1.25	4.0	3.0	35	0.082	0.994
16.0	1.25	4.0	3.0	45	0.123	0.994
16.0	1.25	4.0	3.0	55	0.162	0.996

**Fig. 8** UV-visible spectra of MG oxidized by  $K_2S_2O_8/Ag-Pt$  system at room temperature.

icals. The MG removal efficiency was dropped only 3.4% with 10 mM TBA, suggested that a small quantity of  $HO^{\bullet}$  species were generated. This resulted from the reaction of generated  $SO_4^{\bullet-}$  with water in an aqueous solution. As depicted in Fig. 11A, only ca. 32.4% MG was removed from the reaction solution in presence of 10 mM potassium iodide. These observations can be rationalized due to the presence of numerous  $SO_4^{\bullet-}$  on the surface of Ag-Pt, and the heterogeneous Fenton-like reaction was mainly occurred on the catalyst surface (Wan and Wang, 2017).

The surface stability and catalytic reusability are the two most important capabilities of the using Ag-Pt NPs as persulfate activator for MG oxidation in the Ag-Pt/ $S_2O_8^{2-}$  system. All recycling experiments in this work operated under the same condition: 1.25 mM MG concentration, 4.0 mM  $S_2O_8^{2-}$  concentration, 3.0 pH, 16.0 mg Ag-Pt, and 25  $^{\circ}C$  temperature. Fig. 11B showed that the MG oxidation efficiency was ca. 94.2% after 50 min in the first recycle process, and was over 92.3%, 90.4%, 88.0%, 86.4%, and 85.3% in the next five kinetic runs after 50 min. The above results revealed that the decrease of Ag-Pt activation efficiency may be due to the oxidation of Ag-Pt. The activation of  $S_2O_8^{2-}$  by transition metal and/or NPs to generate reactive  $SO_4^{\bullet-}$  species is not a true catalytic process (Ahn et al., 2019; Zaheer et al., 2023).

In order to compare the persulfate activation efficiency of Ag-Pt with other catalysts, the degradation parameters (time, degradation efficiency, rate constant, and activation energy) of MG are summarized in Table 3. The degradation % and oxidation rates of MG depends on the concentration of MG, pH, amount of catalyst, temperature, and source of light irradiation (Liang, et al., 2017; Lu et al., 2020; Huang, et al., Gokulakrishnan et al., 2012, and Qi, et al. 2017). Table 3 clearly shows that the nature of catalyst, and concentration of  $S_2O_8^{2-}$  have significant impact on the degradation efficiency of MG within a suitable time reaction time. The metal NPs/ $S_2O_8^{2-}$  system is a better approach to generate reactive radicals for the complete degradation of MG and other water contaminants.

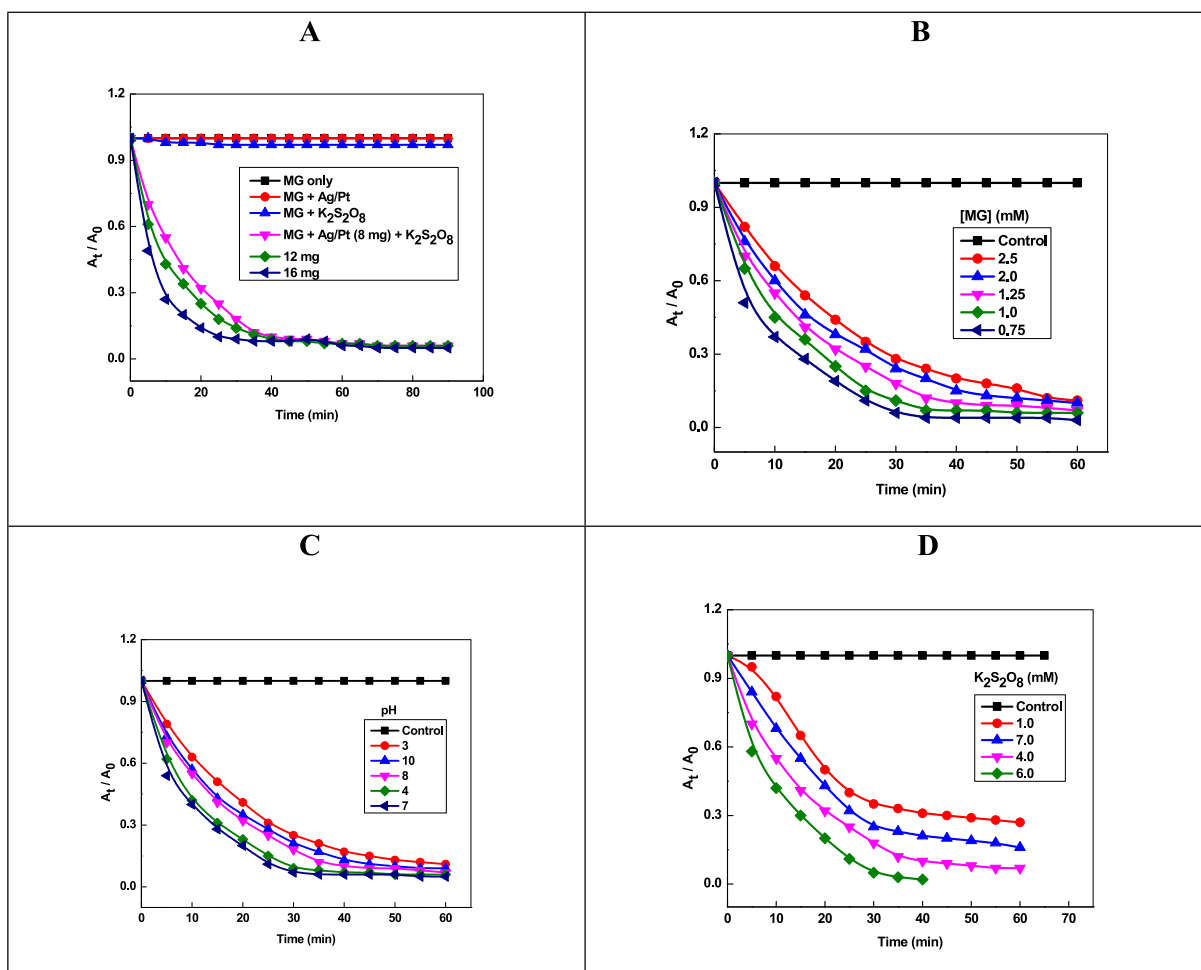
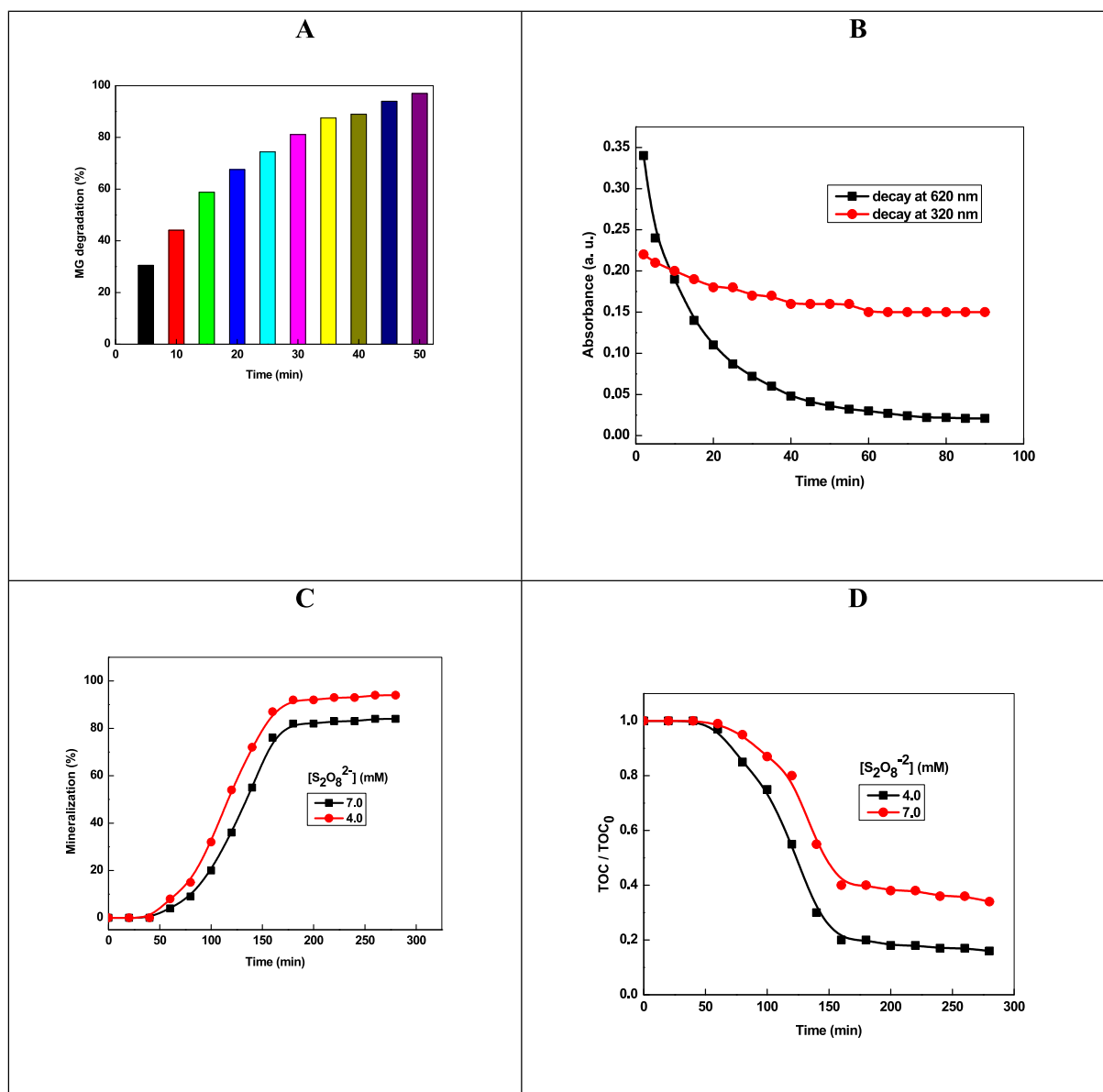


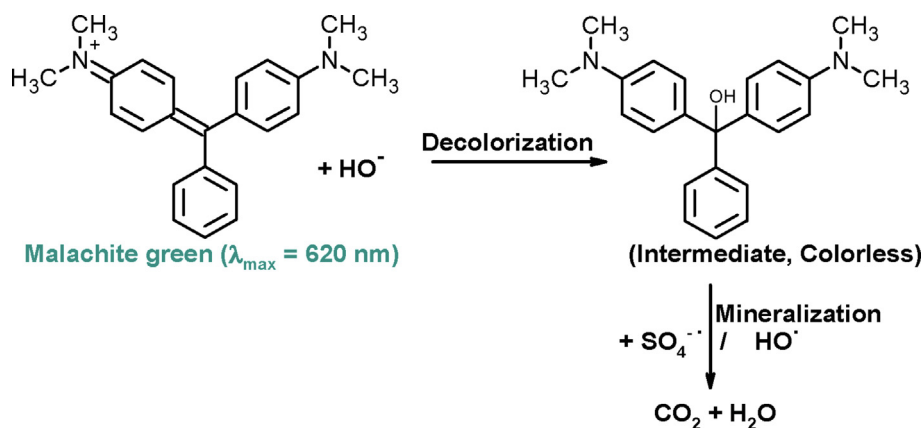
Fig. 9 Effects of Ag-Pt dosage (A), dye concentration (B), initial pH (C), and temperature (D) for activating  $K_2S_2O_8$  to decolorize MG.

**Table 3** Effects of various catalysts on the oxidation of malachite green (MG) by persulfate activation under different experimental conditions.

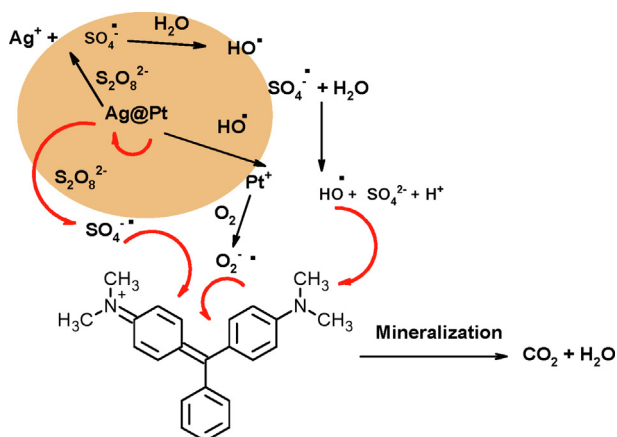
Catalysts	Conditions	Results	Ref.
Fe73.5Si13.5B9Cu1Nb3	[MG] = 22 ppm, catalyst = 0.4 g/L, $[S_2O_8^{2-}] = 1.0$ mM, UV-visible irradiation	Degradation = 100%, Time = 30 min, Rate constant = $0.0849 \text{ min}^{-1}$	Liang, et al., 2017
$Fe_3O_4$ /graphene	[MG] = 20 mg/L, $[S_2O_8^{2-}] = 1.0$ mM, catalyst = 0.2 g/L, T = 25 °C, pH = 3.0, Sun light	Degradation = 91.7%, Time = 12 min, Rate constant = $0.213 \text{ min}^{-1}$	Lu et al., 2020
$Fe_3O_4$ /graphene	[MG] = 20 mg/L, $[S_2O_8^{2-}] = 1.0$ mM, catalyst = 0.2 g/L, T = 25 °C, pH = 3.0, dark	Degradation = 82.18%, Time = 12 min, Rate constant = $0.1474 \text{ min}^{-1}$	Lu et al., 2020
$CuFe_2O_4$ @biochar	[MG] = 100 mg/L, $[S_2O_8^{2-}] = 0.25$ mM, catalyst = 0.2 g/L, T = 25 °C, pH = 7.0	Degradation = 98.9%, Time = 90 min, Rate constant = $0.040 \text{ min}^{-1}$	Huang et al., 2021
Ni(II) perchlorate complex	[MG] = 10 mg/L, $[S_2O_8^{2-}] = 1$ g/L, complex = 200 $\mu\text{M}$ , pH = 7.0	Degradation = 97.9%, Time = 60 min, Rate constant = $0.93 \text{ min}^{-1}$	Gokulakrishnan et al., 2012
CuO	[MG] = 10 $\mu\text{M}$ /L, $[S_2O_8^{2-}] = 250$ $\mu\text{M}$ /L, catalyst = 200 mg/L, pH = 7.0	Degradation = 79.07%, Time = 60 min	Qi et al., 2017
Ag-Pt	[MG] = 1.25 mM, $[S_2O_8^{2-}] = 4.0$ mM, catalyst = 16 mg/L, T = 25 °C, pH = 7.0	Degradation = 94.2%, Time = 50 min, Rate constant = $0.095 \text{ min}^{-1}$ , $E_a = 29.7 \text{ kJ mol}^{-1}$	Present work
$Ag^0$	[MG] = 1.25 mM, $[S_2O_8^{2-}] = 4.0$ mM, catalyst = 16 mg/L, T = 25 °C, pH = 7.0	Degradation = 55.2%, Time = 50 min	Present work
$Pt^0$	[MG] = 1.25 mM, $[S_2O_8^{2-}] = 4.0$ mM, catalyst = 16 mg/L, T = 25 °C, pH = 7.0	Degradation = 0.0%, Time = 30 min	Present work



**Fig. 10** Plots of degradation (A), decay of absorbance (B), TOC percent removal (B), and TOC/TOC<sub>0</sub> (D) for the degradation of MG under K<sub>2</sub>S<sub>2</sub>O<sub>8</sub>/Ag-Pt system. *Reaction conditions:* [MG] = 1.25 mM, and [Ag-Pt] = 16 mg.



**Scheme 7** In situ chemical oxidation of MG by S<sub>2</sub>O<sub>8</sub><sup>2-</sup>/Ag-Pt system.



**Scheme 8** Mechanism of persulfate activation and degradation of MG.

#### 4. Conclusion

Caffeic acid was extracted from an aqueous solution of *Artemisia herba-alba*, and used for the fabrication of stable sols of Ag, Pt, and Ag-Pt NPs at room temperature. The SPR band nature and optical band gap of Ag-Pt NPs were determined by UV-visible spectroscopy. We demonstrated the use of Ag-Pt as heterogeneous  $S_2O_8^{2-}$  activator efficiently, when the initial pH ranged from 3.0 to 10.0. Complete MG decolorization (94.2%) was observed in 50 min reaction time. The MG decomposition percentage increases with amount of Ag-Pt dosage, and reaction temperature. Under optimal conditions ( $[S_2O_8^{2-}]_0 / [dye]_0 = 4.0$  mM, and Ag-Pt dosage = 16 mg), nearly 90% TOC removal of dye can be achieved in 4 h. This study contributes to developing a bimetallic activator for  $SO_4^{\bullet-}$  based advanced oxidation processes in wastewater treatment.

#### Declaration of Competing Interest

The authors declare that they have no known competing financial interests or personal relationships that could have appeared to influence the work reported in this paper.

#### Acknowledgment

This project was funded by the Deanship of Scientific Research (DSR) at the King Abdulaziz University, Jeddah, under grant no. (G-50-247-1441). The authors, therefore, acknowledges with thanks to DSR for technical and financial support.

#### References

- Ahn, Y.-Y., Bae, H., Kim, H.-Il., Kim, S.-H., Kim, J.-H., Leef, S.-G., Lee, J., 2019. Surface-loaded metal nanoparticles for peroxymonosulfate activation: Efficiency and mechanism reconnaissance. *Appl. Catal. B: Environ.* 241, 561-569
- Al-Anazi, A., Abdelraheem, W.H., Han, C., Nadagouda, M.N., Sygellou, L., Arfanis, M.K., Falaras, P., Sharma, V.K., Dionysiou, D.D., 2018. Cobalt ferrite nanoparticles with controlled composition-peroxymonosulfate mediated degradation of 2-phenylbenzimidazole-5-sulfonic acid. *Appl. Catal. B* 221, 266-279.
- Aleboye, A., Olya, M.E., Aleboye, H., 2008. Electrical energy determination for an azo dye decolorization and mineralization by UV/H<sub>2</sub>O<sub>2</sub> advanced oxidation process. *Chem. Eng. J.* 137, 518-524.
- Aljadaani, A. H. A., AL-Thabaiti, S. A., Khan, Z., 2021. SDS capped Cu nanorods: photosynthesis, stability, and their catalytic activity for trypan blue oxidative degradation, *J. Mater. Res. Technol.*, 15, 6841-6854
- Al-Shamaony, L.A., Al-Khazraji, S.M., Twajji, H.A., 1994. Hypoglycemic effect of *Artemisia herba alba* II: effect of a valuable extract on some blood parameters in diabetic animals. *J. Ethnopharmacol.* 43, 167-171.

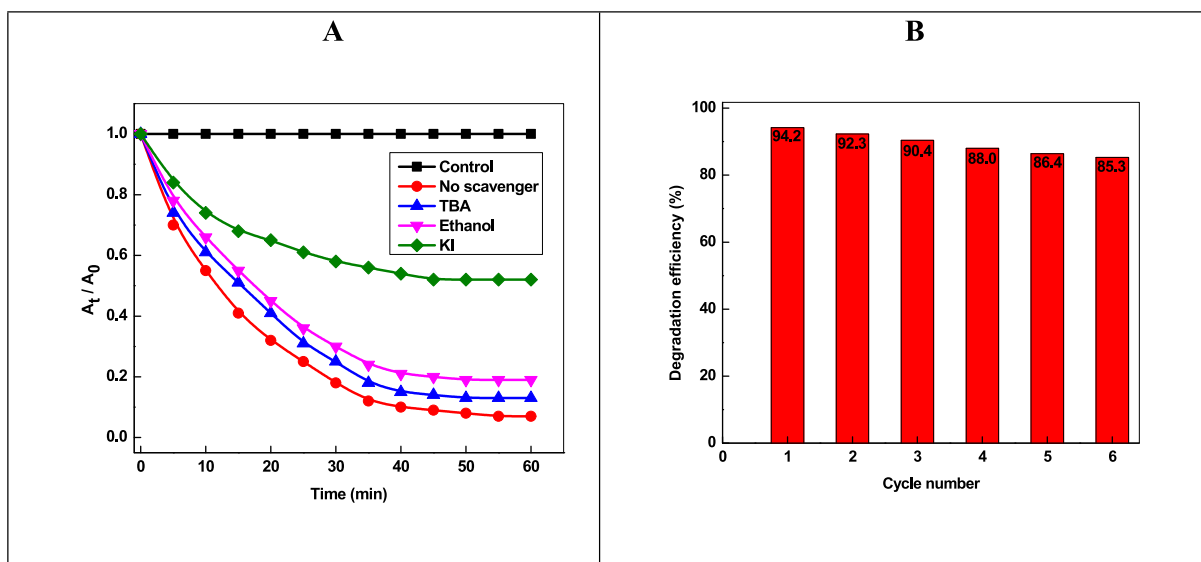


**Fig. 11** Effect of radical scavengers (A) and reusability of Ag-Pt over six cycles (B) on the oxidation of malachite green. *Reaction conditions:* [MG] = 1.25 mM, [Ag-Pt] = 16 mg/L, [K<sub>2</sub>S<sub>2</sub>O<sub>8</sub>] = 4.0 mM, pH = 7.0, Temperature = 25 °C.

- Al-Shamsi, M.A., Thomson, N.R., Forsey, S.P., 2013. Iron based bimetallic nanoparticles to activate peroxygens. *Chem. Eng. J.* 232, 555–563.
- Al-Shehri, A.S., Zaheer, Z., Alsudairi, A.M., Kosa, S.A., 2021. Photo-oxidative Decolorization of brilliant blue with AgNPs as an activator in the presence of  $K_2S_2O_8$  and  $NaBH_4$ . *ACS Omega* 6, 27510–27526.
- Anipsitakis, G., Dionysiou, D., 2004. Radical generation by the interaction of transition metals with common oxidants. *Environ. Sci. Technol.* 38, 3705–3712.
- Asadi, Z., Nami, N., Hosseinzadeh, M., 2018. Green synthesis and characterization of silver nanoparticles (Ag NPs) using white water Lily flower extraction species *Nymphaea Alba* of *Nymphaeaceae* family. *Iran. J. Organ. Chem.* 10, 2403–2408.
- Azmi, W., Sani, R.K., Banerjee, U.C., 1998. Biodegradation of triphenylmethane dyes. *Enzyme Microbial. Technol.* 22, 185–191.
- Bakshi, M.S., 2014. Colloidal micelles of block copolymers as nanoreactors, templates for gold nanoparticles, and vehicles for biomedical applications. *Adv. Colloid Interface Sci.* 213, 1–20.
- Bakshi, M.S., 2018. Engineered nanomaterials growth control by monomers and micelles: From surfactants to surface active polymers. *Adv. Colloid Interface Sci.* 256, 101–110.
- Behnajady, M.A., Modirshahla, N., Shokri, M., Vahid, B., 2008. Effect of operational parameters on degradation of malachite green by ultrasonic irradiation. *Ultrason. Sonochem.* 15, 1009–1014.
- Berberidou, C., Poullos, I., Xekoukoulotakis, N. P., Mantzavinos, D., 2007. Sonolytic, photocatalytic and sonophotocatalytic degradation of malachite green in aqueous solutions. *Appl. Catal. B: Environ.* 74, 63–72.
- Boriky, D., Berrada, M., Talbi, M., Keravis, G., Rouessac, F., 1996. Eudesmanolides from *Artemisia herbaalba*. *Phytochem.* 43, 309–311.
- Cheng, L.-C., Huang, J.-H., Chen, H.M., Lai, T.-C., Yang, K.-Y., Liu, R.-S., Hsiao, M., Chen, C.-H., Here, L.-J., Tsaid, D.P., 2012. Seedless, silver-induced synthesis of star-shaped gold/silver bimetallic nanoparticles as high efficiency photothermal therapy reagent. *J. Mater. Chem.* 22, 2244–2253.
- Colonna, G.M., Caronna, T., Marcandalli, B., 1999. Oxidative degradation of dyes by ultraviolet radiation in the presence of hydrogen peroxide. *Dyes Pigments* 41, 211–220.
- Cornard, J.P., Caudron, A., Merlin, J.C., 2006. UV-visible and synchronous fluorescence spectroscopic investigations of the complexation of Al(III) with caffeic acid, in aqueous low acidic medium. *Polyhedron* 25, 2215–2222.
- Creighton, J.A., Eadon, D.G., 1991. Ultraviolet-visible absorption spectra of the colloidal metallic elements. *J. Chem. Soc. Faraday Trans.* 87, 3881–3891.
- Deng, J., Jiang, J., Zhang, Y., Lin, X., Du, C., Xiong, Y., 2008.  $FeVO_4$  as a highly active heterogeneous Fenton-like catalyst towards the degradation of Orange II. *Appl. Catal. B* 84, 468–473.
- Deng, J., Shao, Y., Gao, N., Deng, Y., Zhou, S., Hu, X., 2013. Thermally activated persulfate (TAP) oxidation of antiepileptic drug carbamazepine in water. *Chem. Eng. J.* 228, 765–771.
- Gardea-Torresdy, J.L., Gomez, E., Videz, J.R.P., Parsons, J.G., Troiani, H., Jose-Yacamán, M., 2003. Alfalfa sprouts: a natural source for the synthesis of silver nanoparticles. *Langmuir* 19, 1357–1361.
- Ghodake, G.S., Deshpande, N.G., Lee, Y.P., Jin, E., 2010. Pear fruit extract-assisted room-temperature biosynthesis of gold nanoplates. *Colloids Surf. B* 75, 584–589.
- Goia, D.V., Matijevic, E., 1998. Preparation of monodispersed metal particles. *New J. Chem.* 22, 1203–1215.
- Gokulakrishnan, S., Parakh, P., Prakash, H., 2012. Degradation of malachite green by potassium persulfate, its enhancement by 1,8-dimethyl-1,3,6,8,10,13-hexaazacyclotetradecane nickel(II) perchlorate complex, and removal of antibacterial activity. *J. Hazard. Mater.* 213–214, 19–27.
- Gu, M., Sui, Q., Farooq, U., Zhang, X., Qiu, Z., Lyu, S., 2018. Degradation of phenanthrene in sulfate radical based oxidative environment by nZVI-PDA functionalized rGO catalyst. *Chem. Eng. J.* 354, 541–552.
- Gulçin, I., 2006. Antioxidant activity of caffeic acid (3,4-dihydroxycinnamic acid). *Toxicology* 217, 213–220.
- Gurtu, A., Akhtar, N., Verma, M., Singh, K., Moyle-Hermann, G., Bakshi, M.S., 2020. Functionalized iron oxide-metal hybrid nanoparticles for protein extraction from complex fluids. *Ind. Eng. Chem. Res.* 59, 1045–1055.
- Hameed, B.H., Lee, T.W., 2009. Degradation of malachite green in aqueous solution by Fenton process. *J. Hazard. Mater.* 164, 468–472.
- Hu, L., Zhang, G., Liu, M., Wang, Q., Dong, S., Wang, P., 2019. Application of nickel foam-supported  $Co_3O_4-Bi_2O_3$  as a heterogeneous catalyst for BPA removal by peroxymonosulfate activation. *Sci. Total Environ.* 647, 352–361.
- Huang, Q., Chen, C., Zhao, X., Bu, X., Liao, X., Fan, H., Gao, W., Hu, H., Zhang, Y., Huang, Z., 2021. Malachite green degradation by persulfate activation with  $CuFe_2O_4@$ biochar composite: efficiency, stability and mechanism. *J. Environ. Chem. Eng.* 9, 105800.
- Iglesias, J., Pazos, M., Andersen, M.L., Skibsted, L.H., Medina, I., 2009. Caffeic acid as antioxidant in fish muscle: mechanism of synergism with endogenous ascorbic acid and alpha-tocopherol. *J. Agric. Food Chem.* 57, 675–681.
- Iravani, S., 2011. Green synthesis of metal nanoparticles using plants. *Green Chem.* 13, 2638–2650.
- Jiang, Z., Zhao, J., Li, C., Liao, Q., Xiao, R., Yang, W., 2020. Strong synergistic effect of  $Co_3O_4$  encapsulated in nitrogen-doped carbon nanotubes on the nonradical-dominated persulfate activation. *Carbon* 158, 172–183.
- Kaveh, S., Norouzi, B., Nami, N., Mirabi, A., 2021. Phytochemical synthesis of CdO nanoparticles: fabrication of electrochemical sensor for quantification of cefixime. *J. Mater. Sci.: Mater. Electron.* 32, 8932–8943.
- Kirubakaran, C.J., Kalpana, D., Lee, Y.S., Kim, A.R., Yoo, D.J., Nahm, K.S., Kumar, G.G., 2012. Biomediated silver nanoparticles for the highly selective copper(II) ion sensor applications. *Ind. Eng. Chem. Res.* 51, 7441–7446.
- Kitching, H., Kenyon, A.J., Parkin, I.P., 2014. The interaction of gold and silver nanoparticles with a range of anionic and cationic dyes. *Phys. Chem. Chem. Phys.* 16, 6050–6059.
- Kosa, S.A., Zaheer, Z., 2019. Betanin assisted synthesis of betanin@silver nanoparticles and their enhanced adsorption and biological activities. *Food Chem.* 298, 125014.
- Laid, M., Hegazy, M-E. F., Ahmed, A. A., 2008. Sesquiterpene lactones from Algerian *Artemisia herbaalba*. *Phytochem. Lett.* 1, 85–88.
- Lau, T.K., Chu, W., Graham, N.J.D., 2007. The aqueous degradation of butylated hydroxyanisole by  $UV/S_2O_8^{2-}$ : study of reaction mechanisms via dimerization and mineralization. *Environ. Sci. Technol.* 41, 613–619.
- Lee, H., Lee, H.-J., Jeong, J., Lee, J., Park, N.-B., Lee, C., 2015. Activation of persulfates by carbon nanotubes: oxidation of organic compounds by nonradical mechanism. *Chem. Eng. J.* 266, 28–33.
- Li, Y., Gao, Z., Ji, Y., Hu, X., Sun, C., Yang, S., Wang, L., Wang, Q., Fang, D., 2015. Photodegradation of malachite green under simulated and natural irradiation: kinetics, products, and pathways. *J. Hazard. Mater.* 285, 127–136.
- Liang, C., H.-W., Su, 2009. Identification of sulfate and hydroxyl radicals in thermally activated persulfate. *Ind. Eng. Chem. Res.* 48, 5558–5562.
- Liang, S.X., Jia, Z., Zhang, W.C., Wang, W.M., Zhang, L.C., 2017. Rapid malachite green degradation using  $Fe_{73.5}Si_{13.5}B_9Cu_1Nb_3$  metallic glass for activation of persulfate under UV-Vis light. *Mater. Design* 119, 244–253.

- Liang, H.-Y., Zhang, Y.-Q., Huang, S.-B., Hussain, I., 2013. Oxidative degradation of p-chloroaniline by copper oxidate activated persulfate. *Chem. Eng. J.* 218, 384–391.
- Liu, W.-J., Qian, T.-T., Jiang, H., 2014. Bimetallic Fe nanoparticles: recent advances in synthesis and application in catalytic elimination of environmental pollutants. *Chem. Eng. J.* 236, 448–463.
- Lu, J., Zhou, Y., Lei, J., Ao, Z., Zhou, Y., 2020. Fe<sub>3</sub>O<sub>4</sub>/graphene aerogels: a stable and efficient persulfate activator for the rapid degradation of malachite green. *Chemosphere* 251, 126402.
- Mohamadi, A.R., Nami, N., Norouzi, B., 2020. Bio-directed synthesis of platinum nanoparticles by *Nymphaea alba* extract: fabrication of a novel non-enzymatic hydrogen peroxide sensor. *J. Mater. Sci.: Mater. Electronics* 31, 18721–18731.
- Naidu, B.R., Venkateswarlu, K., 2022. WEPA: a reusable waste biomass-derived catalyst for external oxidant/metal-free quinoxaline synthesis via tandem condensation–cyclization–oxidation of  $\alpha$ -hydroxy ketones. *Green Chem.* 2022 (24), 6215–6223.
- Oh, S.Y., Kim, H.W., Park, J.M., Park, H.S., Yoon, C., 2009. Oxidation of polyvinyl alcohol by persulfate activated with heat, Fe<sup>2+</sup>, and zero-valent iron. *J. Hazard Mater.* 168, 346–351.
- Okamoto, H., Horii, K., Fujisawa, A., Yamamoto, Y., 2012. Oxidative deterioration of platinum nanoparticle and its prevention by palladium. *Experiment. Dermatol.* 21 (Suppl. 1), 5–7.
- Park, C.M., Heo, J., Wang, D., Su, C., Yoon, Y., 2018. Heterogeneous activation of persulfate by reduced graphene oxide–elemental silver/magnetite nanohybrids for the oxidative degradation of pharmaceuticals and endocrine disrupting compounds in water. *Appl. Catal. B.* 225, 91–99.
- Pouretedal, H.R., Keshavarz, M.H., 2010. Synthesis and characterization of Zn1-XCuXS and Zn1 - XNiXS nanoparticles and their applications as photocatalyst in Congo red degradation. *J. Alloys Compoun.* 501, 130–135.
- Qi, T., Yuru, W., Jinghao, G., Pu, Y., Xiao, Z., Xian, L., 2017. Degradation of malachite green by persulfates activated with CuO. *Chinese J. Environ. Eng.* 11, 2084–2090.
- Ramachandran, K., Kalpana, D., Sathishkumar, Y., Lee, Y.S., Ravichandran, K., Kuamr, G.G., 2016. A facile green synthesis of silver nanoparticles using Piper betle biomass and its catalytic activity toward sensitive and selective nitrite detection. *J. Ind. Eng. Chem.* 35, 29–35.
- Rani, G.J., Rajan, M.A.J., Kumar, G.G., 2017. Reduced graphene oxide/ZnFe<sub>2</sub>O<sub>4</sub> nanocomposite as an efficient catalyst for the photocatalytic degradation of methylene blue dye. *Res. Chem. Intermed.* 43, 2669–2690.
- Riedesel, S., Kaur, R., Bakshi, M.S., 2021. Distinguishing nanoparticle-nanoparticle interactions between gold and silver nanoparticles controlled by gemini surfactants: Stability of nanocolloids. *J. Phys. Chem. C* 125, 5399–5411.
- Saqib, M., Muneer, M., 2003. TiO<sub>2</sub>-mediated photocatalytic degradation of a triphenylmethane dye (gentian violet), in aqueous suspensions. *Dyes Pigments* 56, 37–49.
- Shankar, S.S., Ahmad, A., Pasricha, R., Sastry, M., 2003. Bioreduction of chloroaurate ions by geranium leaves and its endophytic fungus yields gold nanoparticles of different shapes. *J. Mater. Chem.* 13, 1822–1826.
- Sharma, G.D., Shah, M.I., Shahzad, U., Jain, M., Chopra, R., 2021. Exploring the nexus between agriculture and greenhouse gas emissions in BIMSTEC region: the role of renewable energy and human capital as moderators. *J. Environ. Manag.* 297, 113316.
- Singh, R.S., Singh, T., Hassan, M., Larroche, C., 2022. Biofuels from inulin-rich feedstocks: a comprehensive review. *Bioresour. Technol.* 346, 126606.
- Swislocka, R., 2013. Spectroscopic (FT-IR, FT-Raman, UV absorption, 1H and 13C NMR) and theoretical (in B3LYP/6-311++G\*\* level) studies on alkali metal salts of caffeic acid. *Spectrochim. Acta Part A* 100, 21–30.
- Vallinayagam, S., Rajendran, K., Lakkaboyana, S.K., Soontarapa, K., Remya, R.R., Sharma, V.K., Kumar, V., Venkateswarlu, K., Koduru, J.R., 2021. Recent developments in magnetic nanoparticles and nano-composites for wastewater treatment. *J. Environ. Chem. Eng.* 9, 106553.
- Venkateswarlu, K., 2021. Ashes from organic waste as reagents in synthetic chemistry: a review *Environ. Chem. Lett.* 19, 3887–3950.
- Vinothkannan, M., Karthikeyan, C., Kumar, G.G., Kim, A.R., Yoo, D.J., 2015. One-pot green synthesis of reduced graphene oxide (RGO)/Fe<sub>3</sub>O<sub>4</sub> nanocomposites and its catalytic activity toward methylene blue dye degradation. *Spectrochim. Acta A* 136, 256–264.
- Wan, Z., Wang, J., 2017. Degradation of sulfamethazine using Fe<sub>3</sub>O<sub>4</sub>-Mn<sub>3</sub>O<sub>4</sub>/reduced graphene oxide hybrid as Fenton-like catalyst. *J. Hazard. Mater.* 324, 653–664.
- Wang, Z., Zhang, L., Zhao, J., Xing, B., 2016. Environmental processes and toxicity of metallic nanoparticles in aquatic systems as affected by natural organic matter. *Environ. Sci. Nano* 3, 240–255.
- Wang, G.-L., Zhu, X.-Y., Dong, Y.-M., Jiao, H.-J., Wu, X.-M., Li, Z.-J., 2013. The pH-dependent interaction of silver nanoparticles and hydrogen peroxide: a new platform for visual detection of iodide with ultra-sensitivity. *Talanta* 107, 146–153.
- Wu, Y., Zeng, S., Wang, F., Megharaj, M., Naidu, R., Chen, Z., 2015. Heterogeneous Fenton-like oxidation of malachite green by iron-based nanoparticles synthesized by tea extract as a catalyst. *Sep. Puri. Technol.* 154, 161–167.
- Xavier, S. S. J., Kumar, T. R., Ranjani, M., Yoo, D. J., Archana, V., Charles, L., Annaraj, J., G. Kumar, G. G., 2019. Environmentally benign carbon nanodots prepared from lemon for the sensitive and selective fluorescence detection of Fe(III) and tannic acid. *J. Fluoresc.* 29, 631–643
- Xavier, S.S.J., Karthikeyan, C., Kumar, G.G., Kim, A.R., Yoo, D.J., 2014. Colorimetric detection of melamine using  $\beta$ -cyclodextrin-functionalized silver nanoparticles. *Anal. Methods* 6, 8165–8172.
- Xu, X.-R., Li, X.-Z., 2010. Degradation of azo dye orange G in aqueous solutions by persulfate with ferrous ion. *Sep. Puri. Technol.* 72, 105–111.
- Yao, Y., Xu, C., Yu, S., Zhang, D., Wang, S., 2013. Facile synthesis of Mn<sub>3</sub>O<sub>4</sub>-reduced graphene oxide hybrids for catalytic decomposition of aqueous organics. *Ind. Eng. Chem. Res.* 52, 3637–3645.
- Zaheer, Z., Al-Asfar, A., Aazam, E.S., 2019. Adsorption of methyl red on biogenic Ag@Fe nanocomposites adsorbent: Isotherms, kinetics and mechanistic approach. *J. Mol. Liq.* 283, 287–298.
- Zaheer, Z., Al-Shehri, A.S., Alsudairi, A.M., Kosa, S.A., 2023. Silver-ruthenium bimetallic nanoparticles as sacrificial heterogeneous persulfate activator in situ chemical oxidation of dye. *J. Mol. Liq.* 377, 121549.
- Zhang, W.X., Wang, C.B., Lien, H.L., 1998. Treatment of chlorinated organic contaminants with nanoscale bimetallic particles. *Catal. Today* 40, 387–395.
- Zhang, Y., Zhang, B.-T., Teng, Y., Zhao, J., Kuang, L., Sun, X., 2020. Carbon nanofibers supported Co/Ag bimetallic nanoparticles for heterogeneous activation of peroxydisulfate and efficient oxidation of amoxicillin. *J. Hazard. Mater.* 400, 123290.
- Zhu, L., Ai, Z., Ho, W., Zhang, L., 2013. Core-shell Fe-Fe<sub>2</sub>O<sub>3</sub> nanostructures as effective persulfate activator for degradation of methyl orange. *Sep. Purif. Technol.* 108, 159–165.
- Zhu, M., Diao, G., 2011. Synthesis of porous Fe<sub>3</sub>O<sub>4</sub> nanospheres and its application for the catalytic degradation of xylol orange. *J. Phys. Chem. C* 115, 18923–18934.